Increased deformations of aging bone marrow during physical activity is dispensable for cell mechanoresponse in bone analogs

Alex Regner[1*], Maximilien DeLeon[2*], Sean Howard[1], Kalin Gibbons[1], Derek Nesbitt[1], Trevor Lujan[1], Clare Fitzpatrick[1], Mary C Farach-Carson [2], Danielle Wu[2], Gunes Uzer[1 †]

[1] Mechanical and Biomedical Engineering Department, Boise State University

[2] Department of Diagnostic and Biomedical Sciences, UTHealth Science Center at Houston

*co-first author, [†]Corresponding author

Funding support: NIH AG059923, P20GM109095, 5P2CHD086843-03 and NSF 1929188, 2025505.

[†]Corresponding author:

Gunes Uzer PhD

Boise State University

Department of Mechanical & Biomedical Engineering

1910 University Drive, MS-2085

Boise, ID 83725-2085

Ph. (208) 426-4461

Email: gunesuzer@boisestate.edu

Abstract

Aged individuals and astronauts experience bone loss despite rigorous physical activity. Bone mechanoresponse is in-part regulated by mesenchymal stem cells (MSCs) that respond to mechanical challenge. Direct delivery of low intensity vibration (LIV) recovers MSC proliferation in senescence and simulated microgravity models, suggesting that reduced mechanical signal delivery within bone marrow may contribute to declining bone mechanoresponse in aging. To answer this question, we have developed a 3D bone marrow analog that controls trabecular geometry, marrow mechanics and external stimuli. Validated finite element (FE) models were developed to quantify strain environment within hydrogels during LIV. Bone marrow analogs with gyroid-based trabeculae of bone volume fractions (BV/TV) corresponding to adult (25%) and aged (13%) mice were printed using polylactic acid (PLA). MSCs encapsulated in migration-permissive hydrogels within printed trabeculae showed robust cell populations on both PLA surface and hydrogel within a week. Following 14 days of LIV treatment (1g, 100 Hz, 1 hour/day), type-I Collagen and F-actin were quantified for the cells in the hydrogel fraction. While LIV increased all measured outcomes, FE models predicted higher von Mises strains for the 13% BV/TV groups (0.2%) when compared to the 25% BV/TV group (0.1%). Despite increased strains, Collagen-I and F-actin measures remained lower in the 13% BV/TV groups when compared to 25% BV/TV counterparts, indicating that LIV response is does not depend on hydrogel strains and that age-related changes in bone fraction directly affects cell behavior in the hydrogel phase independent of the external stimuli. Overall, bone marrow analogs offer a robust and repeatable platform to study bone mechanobiology.

Key words: Mechanical Signals, Low-Intensity Vibration, Mesenchymal Stem Cells, 3D Printing, Mechanical Modeling, Tissue Modeling

1. Introduction

Mesenchymal stem cells (MSC) found in adult musculoskeletal tissues are responsible for maintaining tissue turnover and repair. In bone, MSC is the common progenitor for osteoblasts, osteocytes and adipocytes.[1-3] During habitual loading, MSCs provide necessary osteoblast populations to facilitate bone modeling.[4] Aging[5-7] and chronic unloading under microgravity[8,9] decrease exercise-induced bone accrual. While aging and unloading phenotypes are associated with decreased proliferative and osteogenic differentiation capacity of MSCs,[10,11] findings from *in vitro* replicative senescence[12] and simulated microgravity models[13] show that exposing MSCs to mechanically active environments improve these outcomes. *In vivo* studies utilizing long daily treadmill activity[14] or ladder climbing regimens[15] also report improved MSC function with long-term physical activity. These studies suggest that reduced mechanical signal delivery to MSCs within the bone marrow due to changes in trabecular volume may contribute to declining bone mechanoresponse in aging and under prolonged unloading. To this end, we sought to develop a 3D bone marrow analog that controls trabecular geometry and external stimuli to study the effects of trabecular bone volume on MSC mechanoresponse.

MSCs in bone exist in a mechanically rich environment. Inside the bone marrow, bone surfaces where bone cells reside, are exposed to matrix deformations[16-19], accelerations[20-25], fluid flow[26-30], and changes in intramedullary pressure[31-33], all of which are inseparable[34]. Cyclic bone deformations associated with walking for example, generates strains up to 400με and fluid velocities up to 100 μm/s within the lacunar–canalicular network [35]. When looking for candidate loading regimens for the bone marrow analog model, we have determined that vibration is the most applicable and practical mechanical input. When a person runs, tibial accelerations reach 2–5g[36] (1g = 9.81 m/s^2), creating complex loading conditions[37] capable of driving MSC function.[38] High frequency and low magnitude signals are also part of bone physiology, measuring 24 hour strain history of load bearing bones across different species showed that bones are subjected to thousands of very small, high frequency strains (< 10 με) during the day.[39] Leveraging the presence of these small strains, application of low intensity vibration (LIV), usually applied between 30 and 100Hz with acceleration magnitudes of 0.1 to 1g, have been utilized in clinical, pre-clinical and cellular studies[4]. In clinical studies, LIV protects bone quantity and quality in women with osteoporosis[40,41], children with cerebral palsy[42], and

improves bone indices in child cancer survivors[43]. Animal studies demonstrate that external LIV application increases trabecular bone density and volume[20], results in stiffer bones [44], and impedes the disuse-induced bone loss[45]. At the cellular level, our group has reported that application of LIV increases MSC contractility [46], activates RhoA signaling [47], and results in increased osteogenic differentiation, as well as increased proliferation of MSCs[48]. Similar to other mechanical signals such as substrate strain, LIV increases the nuclear accumulation of mechanically-sensitive transcription factors, β-catenin[49] and YAP[50] as well as increasing nuclear stiffness[51]. We have recently reported that in a simulated microgravity model where MSCs were exposed to rotating cell culture vessels for 72h to simulate gravitational unloading, LIV rescued YAP nuclear entry induced by RhoA-activator Lysophosphohaditic acid[50].

The mechanical environment LIV generates within the bone marrow is not well studied due to a lack of repeatable model systems. Early modeling efforts utilizing idealized rectangular bone lattices[37] or realistic bone geometries from µCT scans of a human lumbar vertebra[52] reported that LIV can generate fluid shear stress on bone surfaces up to 1-2 Pa depending on the bone marrow viscosity. Follow-up *ex vivo* studies that combined the computational modeling with trabecular explant models under LIV showed that LIV-induced fluid shear were in part correlated with histological findings. However, fluid shear only groups remained lower than the LIV groups[53], suggesting that other mechanical or geometrical factor plays a role. Supporting these findings, our group further reported that LIV effect was largely independent fluid shear in MSCs[48], osteoblasts[54] and osteocytes[55]. While previous studies reveal possible LIV mechanisms, there are no current *in vitro* models to capture the mechanical complexity of bone marrow during mechanical stimulation. Consequently, biological variation and sample availability makes it challenging to setup robust *ex vivo models* to study effect trabecular bone volume using multiple outcomes from identical conditions.

Therefore, to overcome these challenges, we have developed a cell-laden bone marrow analog with a 3D printed PLA trabeculae and hyaluronic acid based bone marrow to quantify the effects of trabecular volume on MSC response during LIV. The bone marrow strains created during 1g, 100Hz vibrations in both 13% and 25% trabecular bone volumes – representing bone volumes of 64 week old (aged) and 8 week old (young) adult male C57BL/6J mouse were compared. Both validated finite element (FE) simulations and *in vitro*

experiments were used to determine whether trabecular bone volume affects the bone marrow mechanical environment and MSC response.

Experimental design

To create a validated experimental bone-analog model, PLA was chosen for the material of the trabecular structure due to its biocompatibility[56] and ease of use in 3D printing applications[57]. Previously developed hyaluronic acid-based hydrogels with MMP cleavable crosslinks and cell attachment sites were chosen to model bone marrow[58]. Primary mouse MSCs dispersed in hydrogels were used as the cell model due to their versatility in both proliferative and differentiation experiments utilized in previous studies[13,16,20,44,45,47-50,59]. To generate an experimentally validated FE model we first utilized a collagen-based gelatin hydrogel (i.e. calibration gels) followed by experiments hyaluronic acid (HA) hydrogel experiments to set model parameters. To capture hydrogel material properties for the FE model validation we employed high-speed compression tests and high-speed speckle photography analysis. Due to large difference in elastic modulus[56,60,61], PLA scaffolds were assumed to be rigid for the purposes of the FE model. Following the FE model validation, idealized 3D trabecular structures based on gyroid model[62] with either 13% or 25% volume fill (i.e. trabecular volume) were generated and LIV-induced HA hydrogel strains were compared between the two trabecular volumes (**Fig.1a**). For *in vitro* experiments (**Fig.1b**), we encapsulated 13% and 25% PLA scaffolds with HA hydrogel-MSC mixture using 1 million cells per mL of hydrogel. Cell-laden hydrogels with no PLA scaffold were used as no-scaffold controls (referred as 0%). Cell-laden 13 and 25% scaffolds exposed to LIV vibration one hour every day at room temperature using 100 Hz frequency and 1g acceleration magnitude. After 14 days, samples were allocated for mRNA (N=4/grp), immunostaining (N=3/grp). Controls were handled the same but were not vibrated.

2. Methods and materials

Preparation of hydrogels

Calibration gels (Knox unflavored Gelatin) or HA hydrogels (Advanced Biomatrix: GS1004) were prepared in 3D PLA printed cylindrical molds with a diameter of 24 mm and a height of 9 mm (**Fig. 2a**). The calibration gels were prepared at 2 mg/ml via dissolving the gelatin powder in 50°C water. Sample molds used for

calibration gels were lined with a thin layer of petroleum jelly to improve mold release and 4.1 ml of 2 mg/ml gelatin mixture was pipetted in. Filled molds were cooled over ice for 1 hour to cross-link and then both the gel and mold were deposited into a room temperature water bath to for 30 minutes. The calibration gel samples were carefully removed from the molds and tested. All tests were completed within 3 hours of initial calibration gel deposition into the molds. HA hydrogels were prepared according to manufacturer protocols. Briefly, degassed (DG) water was extracted via syringe and added to the Glycosil (5.0 ml DG water) and Extralink-Lite (2.5 ml DG water). These were vortexed on a rocker for 60 minutes and vigorously shaken by hand every 15 minutes. These solutions were then combined in a 4:1 ratio (v/v) and mixed by pipette into the mold. These gels cross-linked for 90 minutes at room temperature, removed from the mold, deposited into PBS in 90mm well plate (VWR#10062-878) sealed with parafilm, and left overnight in a 37°C in an incubator, and. The next day the HA hydrogels were tested one at a time, removing them from the PBS immediately prior to testing.

Instantaneous compression testing

Instantaneous compression testing was performed on an INSTRON ElectroPuls E10000 using a 10N load-cell attached to a loading plated with a diameter of 35mm. At the start of each test, calibration and HA gels were placed on water-coated Teflon sheets to prevent adherence (**Fig.2a**). The samples were pre-loaded with 0.025N to ensure full contact with the plate, then compressed to 20% strain (compared to pre-loaded gauge length) at a rate of 90 mm/s. Loading platen position was then held constant for 100 seconds and load-cell data was collected and exported into an excel sheet (**Fig.2b**). The 100 second relaxation data was fitted using a 2-term exponential decay function [$f(x) = ae^{bx} + ce^{dx}$] representing viscoelastic material relaxation. Next, instantaneous force and displacement data was collected during 20% compression at a rate of10.8 mm/s (**Fig.2c**). Compression data then input into MATLAB, converted to stress and strain, and then fit using a 5th order polynomial [$f(x) = ax^5 + bx^4 + cx^3 + dx^2 + ex + f$] representing the instantaneous material behavior. Stress-strain curves for the calibration and HA gels are provided in Supplementary **Fig.S1**.

Digital image correlation tests

Prepared calibration gels were tested in wells with differing width for validating the FE model. The wells with fixed depth (9mm) and height (27.5mm) were 3D printed out of PLA for widths of 4mm, 5mm, 6mm, and 8mm (**Fig. 3a**). These wells were filled with calibration gels as described above and were then speckled with a 50/50 mixture of talc powder and grid 220 silicon carbide (SiC) to track their motions via speckle photometry as previously described[18]. To track light-reflective siC speckles, a white LED light source was used and the motion of the surface was captured with a Photron UX50 high-speed camera at a rate of 2000 frames per second (fps). PLA wells filled with calibration gels were vibrated horizontally at 100Hz with an acceleration of 1G via a custom-made vibration bioreactor driven by a Labworks ET-126HF-1,-4 (13lbf) Electrodynamic transducer using a sinusoidal driving function (**Fig. 3a**). All the vibrations were performed within 3h of gel casting. Recording of gel motion was started 15 seconds post-LIV to ensure that steady state was reached. Recorded high speed videos at 2000fps were analyzed using digital image correlation (DIC) with NCORR software[63] (V1.2) to export gel displacements relative to a moving frame of reference marked on the well surface. Post-processing of the full-field displacement maps were performed in MATLAB. Vibrations were applied along the variable width of the well. For clarity, vibration direction is referred as x-direction and the well height direction is referred as y-direction. During the post-processing of the vibration experiments, the ε_{xx} strain was exclusively analyzed, as it was found to be at least one order of magnitude larger than ε_{yy} or ε_{xy} (see **Fig.S2**). For HA gel experiments, only the 8mm well width was used and same steps were repeated as above. All the experiments were performed in triplicates.

Finite element model generation and validation

An *Altair Hypermesh v2017.2*software package was used to generate the finite element model. 3D printed well geometries between 4 and 8mm were imported as STL files and converted to rigid R3D4 mixed elements with. The hydrogels were meshed using square C3D8R elements with a size of 0.25 mm. C3D8R elements were chosen to prevent hour glassing. These Hypermesh models imported into *ABAQUS (R2019x, Simula, RI)* to simulate vibration. The hydrogel material modelled with a density of 1.0023 g/cm^3 for calibration gels and a density of 1.0018 g/cm^3 for HA gels. Hyperelastic material responses modeled using the procedure outlined by Dalrymple[12]. For viscoelastic modeling, the long-term relaxation was measured starting from the

end of the instantaneous compression to a 100 second interval. This was then fit using a second order exponential function, and data was extrapolated back to 10^{-4} seconds to ensure that ABAQUS was fed data within the rate of vibration (100 Hz). The elastic material definition was modeled as hyperelastic with a 5th order Ogden fit, $U = \sum_{i=1}^{N} \frac{2\mu_i}{\alpha_i^2}\left(\lambda_1^{-\alpha_i} + \lambda_2^{-\alpha_i} + \lambda_3^{-\alpha_i} + \lambda_4^{-\alpha_i} + \lambda_5^{-\alpha_i} - 5\right) + \sum_{i=1}^{N} \frac{1}{D_i}(J^{el} - 1)^{2i}$ where λ_i are principal stretches, N is a parameter (in this case equal to 5), μ_i, α_i, and D_i are temperature dependent material parameters. Using the instantaneous, uniaxial test data (**Fig.1c**), these material definitions were created in ABAQUS.

The material interaction between the undeformable and hydrogel parts used a linear press-overclosure with a slope of 1.0×10^{-2} and a friction and damping coefficients that minimized the difference between experimental and numerical ε_{xx} strain magnitudes at timepoint π/2 using a design of experiments optimization as described below. Mechanical vibration was applied using a connector actuator driven by a periodic velocity equation with an amplitude of 15.61 m/s, and a circular frequency of 100 Hz (628.31 radians).

Damping and friction coefficient optimization

The root mean square error (RMSE) between the time dependent ABAQUS displacement output and the DIC experimental data were calculated using the the ε_{xx} surface strain at the π/2 timepoint of the 8mm well width. To calibrate the friction and damping coefficients in the FE model, a 3 factor 3 level design of experiments (DOE) was performed starting from the measured stiffness value. For the friction and damping coefficients we started with ABAQUS recommended defaults values of 0.75 and 0.03, respectively. Stifness value for the calibration gels varied ±50% of the measured value and the friction and damping coefficients varied between 0.1 -10 and 0.03-0.3, resulting in 27 simulations (**Table 1**). For each comparison, gel surface was divided into a 15x37 grid and for each sub-region the RMSE difference between the experimental and computational ε_{xx} strains were compared. Following this analysis the friction and damping coefficients that minimized the RMSE response was selected (**Fig.4a**). Since increasing or decreasing stiffness from the measured values always resulted in larger RMSE values, 2 factor 3 level DOE was used for the HA gels (**Table S1**) and the friction and damping coefficients that minimized the RMSE response was selected (**Fig.S4a**).

Scaffold finite element modeling

Scaffolds were generated using two bone volumes, 13% and 25%. These respectively correspond to bone volumes of 8 week old (young) and 64 week old (aged) male C57BL/6J mice[64]. Gyroid geometries representing trabecular structures were generated using the equation: $sin(x)cos(y) + sin(y)cos(z) + sin(z)cos(x) < t$, where t is a constant linearly related to the percent volumes[62]. For 13% and 25%, the t scaling value used was -0.121 and -0.752. These models were generated using *MathMod v8.0*, meshed in *Adobe MeshMixer v3.5* using a cell surface density of 128. The models were then scaled to final dimensions of, 5mm x 5mm x 10mm. These were then exported to *Altair Hypermesh v2017.2,* where the STL models were meshed using mixed elements with an element size of 0.14mm. The meshes were made into solid C3D4 elements using tetramesh. The surface of R3D3 elements were exported into ABAQUS.

The FE model was simulated in *ABAQUS (R2019x, Simula, RI).* Pressure-overclosure with a slope of 1.0×10^{-2} was applied to ensure contact between the scaffold and hydrogel surfaces, and both the surface damping and friction coefficients were taken from the optimization procedures. Similar to the previous simulations, the rigid bone was driven by a connector actuator using a periodic velocity equation with an amplitude of 15.61 m/s, and a circular frequency of 100 Hz (628.3 radians). The volumetric strain components corresponding to 13% and 25% scaffolds (ε_{xx}, ε_{yy}, ε_{zz}, ε_{xy}, ε_{yz}, ε_{zx}) were exported. The total hydrogel strain magnitude approximated via equivalent von Mises strain $\varepsilon_{eq} = 2/3\sqrt{3\left(e_{xx}^2 + e_{yy}^2 + e_{xx}^2\right)/2 + 3\left(\gamma_{xy}^2 + \gamma_{yz}^2 + \gamma_{zx}^2\right)/4}$, where engineering strains defined as $\gamma_{ij} = 2x\varepsilon_{ij}$ and deviatoric strains defined as $e_{xx} = +1/2\varepsilon_{xx} - 1/3\varepsilon_{yy} - 1/3\varepsilon_{zz}$, $e_{yy} = -1/3\varepsilon_{xx} + 2/3\varepsilon_{yy} - 1/3\varepsilon_{zz}$, $e_{zz} = -1/3\varepsilon_{xx} - 1/3\varepsilon_{yy} + 2/3\varepsilon_{zz}$.

Scaffold fabrication and application of low intensity vibration

STL files of the 13 and 25% gyroidal scaffolds were 3D printed using PLA on a PRUSA Mk3s 3D printer (PRI-MK3S-KIT-ORG-PEI) with .1mm layer height, and 0.5 x0.5 x1cm overall outer dimensions. These scaffolds were sterilized with Ethylene oxide autoclave for cellular encapsulation.

HA hydrogels integrated with integrin binding motifs (acrylate-PEG-GRGDS) and metalloproteinases (MMPs)-sensitive peptides (PEG-PQ-PEG-acrylate) to encourage adhesion. Cells mixed into the hydrogel at 1×10^6

cells/ml prior to casting and cross-linking. Cell seeded hydrogels were kept for 7 days in growth media in 5% CO_2 and 37ºC to allow growth and attachment prior to experimentation. After 7 days, scaffolds were transferred to two 6 well plates (Corning#3516) with Growth Media (IMDM, 10%FCS and 1% Pen-strep). Scaffolds were oriented identically to the 3D print, and with the long axis orthogonal to the axis of vibration. Scaffolds secured with a custom 3D printed PLA top, and one 3D printed 30mm PLA platen attached to a stainless-steel screw threaded through the top in each well (**Fig.7a**). These ensured the scaffolds would not move during vibration. The scaffolds vibrated for one hour each day, for 14 days. Media changed on day 8.

Immunostaining

Samples were rinsed twice in PBS fixed using 4% paraformaldehyde for 15 minutes at room temperature. Next, they were rinsed 2 times for 5 mins in PBS before being permeabilized in 0.1% triton/PBS for 15 mins at room temperature. All further steps have a 3x10 minute rinse in PBS between them. The scaffolds were separated further to be stained against Collagen-I (*Bioss Antibodies #bs-10423R-A594)*. Based on antibody species, fixed cells blocked using appropriate serum for 30 minutes at room temperature, stained with primary antibody for 1h at 37° C and also labeled against F-actin (1:60 in PBS *Alexa Fluor® 488 Phalloidin-Invitrogen, # A12379*) and DNA (NucBlue, 2 drops/ml, Fisher Scientific #R37605). After a final two rinses for five minutes each, the scaffolds were imaged in PBS using A1R/MP+ Confonfocal/Multiphoton Microscope (Nikon Instruments).

RNA isolation and PCR

Each scaffold was centrifuged at 3000 rpm to separate the gel and scaffolds. Separated gels were added to a single 2 ml tube, and TRIzol™ (*Fisher Scientific#15-596-026*) was added. Gels were mechanically broken up for 30 seconds with a P1000 micropipette and the scaffolds which had been spun to remove the gel were suspended in Zymo lysis buffer and frozen at -80° C overnight. The RNA was then extracted according to manufacturer protocols (Zymo Research #R2071), the RNA extracted from the gel, and scaffold were combined. These RNA samples were then converted to cDNA and PCR analysis was performed for collagen-I using 18s as the control gene. Reverse transcription was performed with 1 µg RNA in a total volume of 20 µl per reaction. 25µL amplification reactions contained primers at 0.5 µm, deoxynucleotide

triphosphates (0.2 mm each) in PCR buffer, and 0.03 U Taq polymerase along with SYBR-green (Molecular Probes, Inc., Eugene, OR) at 1:150,000. mRNA expressions were compared using ΔΔCt method as we previously reported.[48] Samples were run in triplicate. PCR products were normalized for the amount of 18S amplicons. Following primers were used for 18s (Forward-GAACGTCTGCCCTATCAACT, Reverse-CCAAGATCCAACTACGAGCT) and collagen-I (Forward-ATGTGCCACTCTGACTGGAA, Reverse-CAGACGGCTGAGTAGGGAA).

3. Results

Lateral Strain positively correlates with distance during low intensity vibration

High speed visualization of horizontally vibrating wells at 100Hz frequency and 1g acceleration magnitude (**Fig.3b**) showed that the maximum lateral ε_{xx} strain, measured at the peak of the cycle (t= π/2 & t=3π/4), reached to 0.014±0.00047 at 8mm spacing over 5 cycles when averaged across three experiments. The maximum ε_{xx} values were symmetrical on both ends of the well, ensuring that steady state was achieved during measurements (**Fig.3b**). Minimum strains were measured at the end of each positive stroke (t= π). Compared to 8mm at π/2 & t=3π/4 timepoints, averaged maximum ε_{xx} strains of 6mm, 5mm, 4mm well widths were decreased to 0.00806±0.00050 (-0.86%, p=0.66), 0.0075±0.00047 (-7.6%, p=0.17), 0.0030±0.00014 (-62%, p<0.05), respectively (**Fig.3c**). The π/2 sets for each spacing over all three trials were collated into data distribution plots to show the ε_{xx} strains as a function of distance from the well wall. (**Fig.3d**).

Difference between experimental and computational lateral strains are affected by material stiffness as well as friction and damping coefficients

Prior to validating the FE model, we first optimized the model parameters using the experimental data from the 8mm well width experiments. The effect of material stiffness on the average RSME match between DIC experiments and FE models was quantified using the averaged ε_{xx} distribution at the positive and negative peaks. Using experimentally measured stiffness and ABAQUS-recommended default values of 0.75 and 0.03 for the friction and damping coefficients, the average RSME between DIC and FE at π/2 timepoint was 0.19 while the average RMSE between experimental replicates (between the three wells) was 0.15, showing that the average mismatch between FE and DIC was within experimental error. Using default friction and

damping coefficients, increasing or decreasing the measured material stiffness by 50% resulted in average RMSE values of 0.36 and 0.63, which were larger than the experimental variation and indicated the importance of accurate stiffness measurements for modeling.

Since the exact boundary conditions between the gels and the PLA were unknown, we further investigated the possible combinations of friction and damping coefficient values that could further minimize the average RMSE values. Varying the friction coefficient between 10 and 0.1 resulted in the average RMSE values of 0.28 and 0.16 at measured stiffness and default damping coefficient. Similarly, only varying damping coefficient between values of 0.3 and 0.003 resulted in average RMSE values of 0.28 and 0.3, respectively. Since the gel stiffness was measured experimentally, an empirical linear DOE model using a 2nd order polynomial was used to find the optimal friction / damping combination (**Table 1**). The lowest average RMSE of 0.16 obtained at the friction / damping combination of 0.1/0.003, gel which was not further decreased by the DOE model. Shown by the 15x37 RMSE grid (**Fig.4a**), maximum difference between the experimental- and FE-derived ε_{xx} magnitudes were largest towards the outer walls. Of this, the largest RMSE difference of 0.015 occurs in the regions 5 and 6. Match in regions 3 and 4 were closer, an averaged difference of 0.0047 and 0.0052, respectively. Differences in corner regions 1, 2, 5 and 6 were 0.0077, 0.0079, 0.0113, and 0.0122, respectively. RMSE grid for the HA gels is shown in the supplementary **Fig.S4**. The largest RMSE difference of 0.024 again occurs in region 6, with regions 3 and 4 (the middle regions) matching the closest with ε_{xx} averages of .0091 and 0.0082, respectively. Differences in corner regions 1, 2, 4, & 5 were 0.011, 0.010, 0.010, and 0.098, respectively.

Using the friction / damping coefficient combinations that minimized the average RMSE values between DIC and FE results at 8mm well width, we have quantified the averaged ε_{xx} magnitudes over 6mm, 5mm, and 4mm for the calibration gel (**Fig.5a**). The maximum ε_{xx} values were symmetrical at both the $\pi/2$ and $t=3\pi/4$, in addition to both ends of the well, demonstrating steady state (**Fig.5b**). The $\pi/2$ sets for each spacing over all three trials collated into data distribution plots (**Fig.5c**), which showed increasing extrema differences as the spacing decreased from 8mm. When compared to 8mm, the averaged maximum ε_{xx} strains of 6mm, 5mm and 4mm well widths decreased to 0.017±0.00040 (-22%, $p<0.05$), 0.013±0.00030 (41%, $p<0.05$),

0.010±0.00037 (-54%, $p<0.05$) , and 0.0026±0.00051 (-88%, $p<0.05$), respectively . Plotting ε_{xx} strains as function of distance from the well wall showed a similar distribution to DIC data. (**Fig.4d**).

Low trabecular volumes increase LIV-induced hydrogel strains

We next compared the 3D strain distribution between 13% and 25% scaffolds under LIV (**Fig.6a**) using HA gel mechanical properties. Comparing the Von Mises strain (ε_{VM}) magnitude averaged over steady-state cycles showed that ε_{VM} of 25% was 50% smaller compared to 13% scaffold (**Fig. 6b**, $p<0.0001$). ε_{VM} distribution (**Fig.6c**) indicated normally distributed strains for both 13% and 25% scaffolds. Histograms of 25% and 13% scaffolds were statistically different ($p<0.05$), 25% scaffold had more elements with lower strain values while 13% scaffold showed elements with higher ε_{VM} strains. Comparing individual strain components, showed a significant difference ($P< 0.05$) between ε_{zz}, ε_{xy} and ε_{yz} strains, no differences were found between ε_{xx}, ε_{yy}, and ε_{zx} strains. Min/Max values for the normal (εxx, ε_{yy} and ε_{zz}) and shear (εxy, ε_{yz} and ε_{zx}) components are given in **Table 2**.

Bone Analogs show viable cells with two distinct cell populations

In order to compare the possible differences in MSC mechanoregulation due to bone volume differences we generated two sets of PLA scaffolds (13% and 25% volume fill) and 0% controls. Cell-laden 13 and 25% scaffolds vibrated one hour every day at room temperature using 100Hz frequency or 1g acceleration magnitude (**Fig.7a**). Controls were kept outside of the incubator but not vibrated. After 14 days, samples were allocated for qPCR (N=4 scaffolds/grp), imaging (N=3 scaffolds/grp). Live/dead straining prior to start of the experiments at day 0 (7 days post-encapsulation) showed viable cells on both PLA and in hydrogels (**Fig.7c**). Shown in **Fig.7d**, morphology of cells on PLA surfaces were similar to 2D culture plates (**Fig.S5**), showing elongated morphology while cells in hydrogels were smaller and more rounded (**Fig.7e**).

LIV increases F-actin volume independent of hydrogel strains

We first tested the F-actin volume in hydrogels in response to LIV using samples stained against Phalloidin. Comparing 0%, 13% and 25% samples without LIV showed no significant change in the F-actin volume. Shown in **Fig.8b**, comparing -LIV samples with their +LIV counterparts we found that 13% BV/TV group with

a larger hydrogel strain (average ε_{VM} 0.02%, **Fig.6b**) had trend toward increasing F-actin (+50%, ns) while 25% BV/TV with a lower hydrogel strain (average ε_{VM} 0.01%, **Fig.6b**) showed a 2.4-fold increase ($p<0.05$), suggesting that LIV effect is independent of the hydrogel strain.

Trabecular volume differentially regulates basal and LIV-induced collagen-I production

Collagen-I immunostaining showed a more robust collagen labeling in vibrated samples (+LIV), when compared to non-vibrated controls (-LIV, **Fig.8a-b**). Collagen-I mRNA quantification showed a trend of increased collagen-I expression in +LIV samples (+50% in 13% and +94% in 25% samples, **Fig.5c**). Quantification collagen-I from volumetric scans showed unchanged basal collagen-I levels between 0% and 13% controls while -LIV 25% group had a 73% increase compared to -LIV 13% group ($p<0.05$). LIV increased collagen-I in both 13% and 25% groups by 87% and 53% respectively ($p<0.01$) and +LIV 25% remained significantly higher compared to +LIV 13% group (37%, $p<0.05$).

4. Discussion

We have found that hydrogel strain magnitudes between scaffolds representing young (25%) and aged (13%) trabecular volumes significantly differ during LIV. Validation studies indicating that strain magnitude within the LIV direction is positively correlated with the spacing between two solid structures (**Fig. 3d& 5c**). This conclusion also supported when comparing 25% and 13% scaffolds: Average ε_{VM} for the 25% scaffold was 50% smaller when compared to the 13% scaffold which had more spacing between trabecular struts (**Fig. 6a-b**). These findings indicate that age-related bone adaptations, decreased trabecular volume and increased cortical circumference[65] may serve to increase the magnitude of bone marrow deformation during physical activity.

In contrast to larger hydrogel strains observed F-actin volumes (**Fig.8**) and Collagen-I production (**Fig.9**) of 13% scaffolds remained behind when compared to 25% scaffolds. The fact that LIV-induced outcomes were lower in 13% scaffolds we conclude that LIV response is relatively insensitive to hydrogel strains. This insensitivity of LIV response to scaffold type can be due to several reasons. First, measured strain

differences within the hydrogel only represents a fraction of the mechanical information. During 1g, 100Hz sinusoidal vibrations the entire scaffold - including PLA surfaces and hydrogel - accelerates and decelerates to speed of ±15mm/s, 100 times each second, providing another mechanical input in addition to LIV-induced hydrogel strains. We have previously reported that when substrate strains are extremely low, LIV activates COX-2 signaling in MC3T3 osteoblasts[54], improves gap junctional communication in MLO-Y4 osteocytes[55] and increases proliferation as well as collagen biosynthesis related proteins in MSCs under simulated microgravity[13]. While this suggest that LIV could be regulating collagen production and changes in F-actin independent of hydrogel strains, it does not immediately explain why 25% scaffolds show more collagen production when compared to 13% scaffolds and 0% controls.

Another possibility is the differences in scaffold surface area. Due to increased bone volume, the 25% scaffolds had a larger scaffold surface area, increasing the possibility that imaging regions are closer to the walls. Confocal images showed many cells that were viable and spread on the PLA surfaces (**Fig.7**). While our analysis excluded cells on the PLA surface from the data, these cells on PLA surfaces may produce paracrine signals to cells within the hydrogels. For example, during bone remodeling, early stage osteoblast lineage cells that reside on bone surfaces are at a low cell density but their density increases during the reversal phase [66]. Interestingly, early osteoblast lineage cells are “pro-resorptive” (high RANKL, low OPG, high SMA and MMP13), and that osteoid deposition start only when a critical cell density is reached [67]. This suggest that basal and LIV-driven density changes of these PLA surface cells would not only signal to hydrogels cells but may also regulate important factors such YAP/TAZ that change their localization based on cell density[68]. While the metrics of this population was not investigated in this study, future studies aimed at possible interactions of cells on the PLA surface and hydrogel will be important.

Despite our attempts there was a difference between our DIC experimental data and our FE model, in both our calibration and HA gels. Highlighting the inherent variation in DIC experiments, the average RMSE values between calibration or HA experiment were close to differences between experimental data and computational models. A couple factors that may have contributed to this variability. The first has to do with the rigid body assumption we assigned to PLA in our simulations. While this appears to be a valid assumption

and used by others[56], there is a potential model limitation for not accounting for strain damping that the walls, that may decrease the wall strain in the FE model. Another source of error is the DIC method itself, where the PLA-hydrogel boundaries cannot be resolved via optical resolution, resulting lower averages at the boundaries when compared to FE model, where resolution is numerical. Therefore, this limitation of DIC could be under-estimating the magnitudes towards the walls of the model.

In this study we have developed a bi-phasic bone analogs with fully characterized hydrogel strain environment during low intensity vibrations. Our findings show that trabecular densities associated with advanced age results in higher hydrogel strains while trabecular densities expected at adulthood results in smaller strains during LIV. Despite the lower strain magnitudes, young bone marrow is able to support higher cell proliferation and collagen production at both basal and mechanically stimulated scaffolds, suggesting that factors other than hydrogel environment is at play. These findings not only open up interesting new avenues of research to study interaction between scaffold-lining and hydrogel encapsulated cells to mimic bone marrow mechanobiology, the model itself establishes a versatile 3D platform to study how mechanical signals may affect multi-cellular processes such as cancer metastasis to bone and environmental factors such as microgravity and radiation.

Data availability

The datasets generated and/or analyzed during the current study are available from the corresponding author on reasonable request.

Acknowledgements

Awards from NIH R01AG059923, P20GM109095, 5P2CHD086843-03 and NSF 1929188, 2025505, supported this study.

Competing interests

The author(s) declare no competing interests financial or otherwise.

Author Contributions

Alex Regner: concept/design, data analysis/interpretation, manuscript writing

Maximilien DeLeon: concept/design, data analysis/interpretation, manuscript writing

Sean Howard: concept/design, data analysis, manuscript writing, final approval of manuscript

Kalin Gibbons: concept/design, manuscript writing, final approval of manuscript

Derek Nesbitt: data analysis, final approval of manuscript

Trevor Lujan: data analysis, final approval of manuscript

Clare Fitzpatrick manuscript writing, data analysis, financial support, final approval of manuscript

Mary C Farach-Carson: manuscript writing, financial support, final approval of manuscript

Danielle Wu: manuscript writing, data analysis, financial support, final approval of manuscript

Gunes Uzer: concept/design, data analysis/interpretation, financial support, manuscript writing, final approval of manuscript

Figure 1. Experimental Design

Figure 2. Mechanical Characterization Setup. a) Timeline of the compression testing, with all tests completed within 3 hours of initial gelation for the calibration gels. 3D printed mold used to cast instantaneous gel pucks (24mm internal diameter, and a height of 9mm). Experiments were completed using an INSTRON ElectroPuls E10000 using a 10N load-cell. The sample rested on a Teflon coated sheet lightly coated in water to prevent adherence. **b)** Relaxation data over a 100 second time period (blue) and the resulting fit line (red) relaxing from 2.8×10^{-5} MPa and reaching long term relaxation at approximately 2.1×10^{-5} Mpa. **c)** Instantaneous ramp data from 12 trials (dotted 5th order polynomial fit (blue), compressed to 0.2 strain (10.8 mm/s).

Figure 3. Model validation experiments. a) Timeline of the DIC tests, with all tests completed within 3 hours of initial gelation for the calibration gels. Hydrogels were speckled with 220 grid SiC and the camera recorded the motions at 2000 frames per second (fps). Horizontal vibration plate was driven by Labworks

ET-126HF-1,-4 (13lbf) Electrodynamic transducer **b)** A PLA experimental setup was manufactured to visualize strain during100Hz -1g vibrations at the horizontal direction. ε_{xx} strains varied periodically with the maximum value of 0.015 at 8mm spacing **c)** As the spacing decreased 62% to 4mm ε_{xx} strain decreased by two orders of magnitude showing a positive, non-linear correlation in the average maximum of the strain **d)** Mapping max strain magnitudes from the wall to the mid-point showed a convex parabolic strain profile that minimized at the middle.

Figure 4 RMSE difference between DIC and FE strains . a) The difference between the surface of DIC experimental and the FE model was measured with a 15x37 grid and divided into 6 regions for comparison. Most of the difference occurs on the outside, especially the outer edges. **b)** Largest difference of 0.015 of averaged ε_{xx} magnitude difference occurs in the regions 5 and 6. Regions 3 and 4 are the closest matching, with an averaged ε_{xx} magnitude difference of 0.0047 and 0.0052, respectively. The corner regions (1, 2, 5 and 6) has an averaged ε_{xx} magnitude difference of 0.0077, 0.0079, 0.0113, and 0.0122, respectively.

Figure 5. Model validation simulations a) Finite Element (FE) model setup with 8mm wall spacing. Wells were vibrated identically to the experiments (Fig.3). Each FE run was proceeded by a gravity step **b)** ε_{xx} strain magnitude over the cycle. maximum ε_{xx} values were symmetrical at both the $\pi/2$ and $3\pi/4$, in addition to both ends of the well, demonstrating steady state **c)** . Extrema differences were evenly spaced as the spacing changes. When compared, the surface strain at the 8mm between the averaged maximum ε_{xx} strains of 6mm, 5mm and 4mm well widths decreased to 0.017±0.00040 (-22%, $p<0.05$), 0.013±0.00030 (41%, $p<0.05$), 0.010±0.00037 (-54%, $p<0.05$) , and 0.0026±0.00051 (-88%, $p<0.05$), **d)** Mapping the maximum strain magnitudes, we see a convex parabolic curve with each spacing, excluding 8mm.

Figure 6. Low trabecular volumes increase LIV-induced hydrogel strains. a) We compared the 3D strain distribution between 13% and 25% scaffolds under LIV using HA gel mechanical properties (Table S1). **b)** Comparing the Von Mises strain (ε_{VM}) magnitude averaged over steady-state cycles showed that εVM of 13% was almost doubled compared to 25% scaffold ($p<0.0001$). **c)** ε_{VM} distribution indicated normally distributed strains for both 13% and 25% scaffolds. Histograms of 25% and 13% scaffolds were statistically different

(p<0.05)., 25% scaffold had more elements with lower strain values while 13% scaffold showed elements with higher ε_{VM} strains.

Figure 7. Bone Analogs show viable cells with two distinct cell populations. a) Two sets of PLA scaffolds (13% and 25% volume fill) and 0% controls were generated. Cell-laden 13% and 25% scaffolds were vibrated one hour every day at room temperature using 100 Hz frequency and 1g acceleration magnitude outside of the incubator. After 14 days, samples were allocated for qPCR (N=4 scaffolds/grp), imaging (N=3 scaffolds/grp) **b)** PLA surface provides an ideal surface for cell attachment **c)** Utilizing live/dead straining to detect cell viability prior to start of the experiments at 7 days post-encapsulation showed viable cells on both PLA and in hydrogels. **d)** Morphology of cells on PLA surfaces were similar to 2D culture plates (Fig.S5), showing elongated morphology while cells in e) hydrogels were smaller and more rounded.

Figure 8. LIV increases F-actin volume F-actin staining in **a)** 25% scaffolds show increased F-actin volume in +LIV samples when compared to controls (-LIV). **b)** Quantification F-actin volume showed no change in -LIV groups. 13% +LIV groups had a trend toward increased F-actin and 25% +LIV group showed 2.5-fold increase in F-actin volume (p<0.05).

Figure 9. Trabecular volume differentially regulates basal and LIV-induced regulates collagen-I production Collagen-I immunostaining in **a)**13% and 25% scaffolds show an increased collagen labeling in vibrated samples (+LIV), vs non vibrated controls (-LIV). **b)** Collagen-I mRNA quantification show an increasing trend of collagen-I expression in +LIV samples (+50% in 13% and +94% in 25% samples. Everything was normalized to 0% controls (shown as the dashed gray bar) **c)** Quantification Collagen-I volume showed unchanged basal collagen-I levels between 0% and 13% controls while -LIV 25% group had a 73% increase compared to -LIV 13% group (p<0.05). LIV increased Collagen-I in both 13% and 25% groups by 87% and 53% respectively (p<0.01) and +LIV 25% remained significantly higher compared to +LIV 13% group (37%, p<0.05).

Table 1: DOE factors used to minimize RMSE between *in vitro* and *in silico* results for calibration gels

Stiffness	Friction	Damping	RMSE
1.5	10	0.3	0.41
1.5	10	0.003	0.37
1.5	10	0.03	0.47
1.5	0.1	0.3	0.50
1.5	0.1	0.003	0.38
1.5	0.1	0.03	0.38
1.5	0.75	0.3	0.35
1.5	0.75	0.003	0.36
1.5	0.75	0.03	0.36
0.5	10	0.3	0.53
0.5	10	0.003	0.45
0.5	10	0.03	0.56
0.5	0.1	0.3	0.58
0.5	0.1	0.003	0.50
0.5	0.1	0.03	0.49
0.5	0.75	0.3	0.63
0.5	0.75	0.003	0.64
0.5	0.75	0.03	0.63
1	10	0.3	0.29
1	10	0.003	0.28
1	10	0.03	0.28
1	0.1	0.3	0.16
1	0.1	0.003	0.16
1	0.1	0.03	0.16
1	0.75	0.3	0.30
1	0.75	0.003	0.28
1	0.75	0.03	0.19

Table 2: *In silico* comparison of directional strains between 13% and 25% scaffolds during LIV.

Tensor	13%		25%	
	Min	Max	Min	Max
XX	-0.053	0.062	-0.047	0.012
YY	-0.056	0.071	-0.017	0.050
ZZ	-0.075	0.067	-0.047	0.029
XY	-0.102	0.067	-0.023	0.025
YZ	-0.082	0.104	-0.042	0.053
ZX	-0.078	0.089	-0.021	0.062

Table S1: DOE factors used to minimize RMSE between *in vitro* and *in silico* results for HA gels

Friction	Damping	RMSE
10	0.3	0.28
10	0.003	0.29
10	0.03	0.28
0.1	0.3	0.38
0.1	0.003	0.25

0.1	0.03	0.35
0.75	0.3	0.28
0.75	0.003	0.28

References

1 Krishnan, V., Bryant, H. U. & MacDougald, O. A. Regulation of bone mass by Wnt signaling. *J.Clin.Invest* **116**, 1202-1209 (2006).

2 Menuki, K. *et al.* Climbing exercise enhances osteoblast differentiation and inhibits adipogenic differentiation with high expression of PTH/PTHrP receptor in bone marrow cells. *Bone* **43**, 613-620 (2008).

3 David, V. *et al.* Mechanical loading down-regulates peroxisome proliferator-activated receptor gamma in bone marrow stromal cells and favors osteoblastogenesis at the expense of adipogenesis. *Endocrinology* **148**, 2553-2562 (2007).

4 Pagnotti, G. M. *et al.* Combating osteoporosis and obesity with exercise: leveraging cell mechanosensitivity. *Nature Reviews Endocrinology*, doi:10.1038/s41574-019-0170-1 (2019).

5 Cabahug-Zuckerman, P. *et al.* Site-Specific Load-Induced Expansion of Sca-1+Prrx1+ and Sca-1−Prrx1+ Cells in Adult Mouse Long Bone Is Attenuated With Age. *JBMR Plus* **3**, e10199, doi:https://doi.org/10.1002/jbm4.10199 (2019).

6 Fafian-Labora, J. *et al.* Influence of age on rat bone-marrow mesenchymal stem cells potential. *Scientific reports* **5**, 16765, doi:10.1038/srep16765 (2015).

7 Razi, H. *et al.* Aging Leads to a Dysregulation in Mechanically Driven Bone Formation and Resorption. *J Bone Miner Res* **30**, 1864-1873, doi:10.1002/jbmr.2528 (2015).

8 Bikle, D. D., Halloran, B. P. & Morey-Holton, E. Impact of skeletal unloading on bone formation: Role of systemic and local factors. *Acta Astronautica* **33**, 119-129 (1994).

9 Greenleaf, J. E., Bulbulian, R., Bernauer, E. M., Haskell, W. L. & Moore, T. Exercise-training protocols for astronauts in microgravity. *Journal of applied physiology (Bethesda, Md. : 1985)* **67**, 2191-2204, doi:10.1152/jappl.1989.67.6.2191 (1989).

10 Puts, R., Albers, J., Kadow-Romacker, A., Geissler, S. & Raum, K. Influence of Donor Age and Stimulation Intensity on Osteogenic Differentiation of Rat Mesenchymal Stromal Cells in Response to Focused Low-Intensity Pulsed Ultrasound. *Ultrasound in medicine & biology* **42**, 2965-2974, doi:10.1016/j.ultrasmedbio.2016.08.012 (2016).

11 Maredziak, M., Marycz, K., Tomaszewski, K. A., Kornicka, K. & Henry, B. M. The Influence of Aging on the Regenerative Potential of Human Adipose Derived Mesenchymal Stem Cells. *Stem cells international* **2016**, 2152435, doi:10.1155/2016/2152435 (2016).

12 Bas, G. *et al.* Low Intensity Vibrations Augment Mesenchymal Stem Cell Proliferation and Differentiation Capacity during in vitro Expansion. *Scientific reports* **10**, 9369, doi:10.1038/s41598-020-66055-0 (2020).

13 Touchstone, H. *et al.* Recovery of stem cell proliferation by low intensity vibration under simulated microgravity requires intact LINC complex *npj. Microgravity* **5**, doi:doi.org/10.1038/s41526-019-0072-5 (2019).

14 Hell, R. C. R. *et al.* Physical activity improves age-related decline in the osteogenic potential of rats' bone marrow-derived mesenchymal stem cells. *Acta Physiologica* **205**, 292-301, doi:10.1111/j.1748-1716.2011.02397.x (2012).

15 Singulani, M. P. *et al.* Effects of strength training on osteogenic differentiation and bone strength in aging female Wistar rats. *Scientific reports* **7**, 42878, doi:10.1038/srep42878 (2017).

16 Rubin, C. T. & Lanyon, L. E. Regulation of bone mass by mechanical strain magnitude. *Calcified tissue international* **37**, 411-417 (1985).

17 O'Connor, J. A., Lanyon, L. E. & MacFie, H. The influence of strain rate on adaptive bone remodelling. *Journal of biomechanics* **15**, 767-781 (1982).

18 Rath, B., Nam, J., Knobloch, T. J., Lannutti, J. J. & Agarwal, S. Compressive forces induce osteogenic gene expression in calvarial osteoblasts. *Journal of biomechanics* **41**, 1095-1103, doi:10.1016/j.jbiomech.2007.11.024 (2008).

19 Poliachik, S. L., Threet, D., Srinivasan, S. & Gross, T. S. 32 wk old C3H/HeJ mice actively respond to mechanical loading. *Bone* **42**, 653-659, doi:10.1016/j.bone.2007.12.222 (2008).

20 Rubin, C., Turner, A. S., Bain, S., Mallinckrodt, C. & McLeod, K. Anabolism. Low mechanical signals strengthen long bones. *Nature* **412**, 603-604, doi:10.1038/35088122 (2001).

21 Oxlund, B. S., Ortoft, G., Andreassen, T. T. & Oxlund, H. Low-intensity, high-frequency vibration appears to prevent the decrease in strength of the femur and tibia associated with ovariectomy of adult rats. *Bone* **32**, 69-77, doi:10.1016/s8756-3282(02)00916-x (2003).

22 Tanaka, S. M. *et al.* Effects of broad frequency vibration on cultured osteoblasts. *J Biomech* **36**, 73-80 (2003).

23 Garman, R., Gaudette, G., Donahue, L. R., Rubin, C. & Judex, S. Low-level accelerations applied in the absence of weight bearing can enhance trabecular bone formation. *Journal of orthopaedic research : official publication of the Orthopaedic Research Society* **25**, 732-740, doi:10.1002/jor.20354 (2007a).

24 Wren, T. A. *et al.* Effect of high-frequency, low-magnitude vibration on bone and muscle in children with cerebral palsy. *J Pediatr Orthop* **30**, 732-738, doi:10.1097/BPO.0b013e3181efbabc (2010).

25 Pre, D. *et al.* The differentiation of human adipose-derived stem cells (hASCs) into osteoblasts is promoted by low amplitude, high frequency vibration treatment. *Bone* **49**, 295-303, doi:10.1016/j.bone.2011.04.013 (2011).

26 McGarry, J. G., Klein-Nulend, J., Mullender, M. G. & Prendergast, P. J. A comparison of strain and fluid shear stress in stimulating bone cell responses--a computational and experimental study. *FASEB journal : official publication of the Federation of American Societies for Experimental Biology* **19**, 482-484, doi:10.1096/fj.04-2210fje (2005).

27 Sikavitsas, V. I., Bancroft, G. N., Holtorf, H. L., Jansen, J. A. & Mikos, A. G. Mineralized matrix deposition by marrow stromal osteoblasts in 3D perfusion culture increases with increasing fluid shear forces. *Proc Natl Acad Sci U S A* **100**, 14683-14688, doi:10.1073/pnas.2434367100 (2003).

28 Bancroft, G. N. *et al.* Fluid flow increases mineralized matrix deposition in 3D perfusion culture of marrow stromal osteoblasts in a dose-dependent manner. *Proceedings of the National Academy of Sciences of the United States of America* **99**, 12600-12605, doi:10.1073/pnas.202296599 (2002).

29 Weinbaum, S., Cowin, S. C. & Zeng, Y. A model for the excitation of osteocytes by mechanical loading-induced bone fluid shear stresses. *J Biomech* **27**, 339-360 (1994).

30 Reich, K. M., Gay, C. V. & Frangos, J. A. Fluid shear stress as a mediator of osteoblast cyclic adenosine monophosphate production. *J Cell Physiol* **143**, 100-104, doi:10.1002/jcp.1041430113 (1990).

31 Qin, Y. X. & Hu, M. Intramedullary pressure induced by dynamic hydraulic pressure stimulation and its potential in treatment of osteopenia. *Bone* **48**, S186-S186, doi:10.1016/j.bone.2011.03.432 (2011).

32 Qin, Y. X. & Lam, H. Y. Intramedullary pressure and matrix strain induced by oscillatory skeletal muscle stimulation and its potential in adaptation. *Journal of biomechanics* **42**, 140-145, doi:10.1016/j.jbiomech.2008.10.018 (2009).

33 Zhang, P., Su, M., Liu, Y. L., Hsu, A. & Yokota, H. Knee loading dynamically alters intramedullary pressure in mouse femora. *Bone* **40**, 538-543, doi:10.1016/j.bone.2006.09.018 (2007).

34 Birks, S. & Uzer, G. At the nuclear envelope of bone mechanobiology. *Bone* **151**, 116023, doi:10.1016/j.bone.2021.116023 (2021).

35 Price, C., Zhou, X., Li, W. & Wang, L. Real-time measurement of solute transport within the lacunar-canalicular system of mechanically loaded bone: direct evidence for load-induced fluid flow. *J Bone Miner Res* **26**, 277-285, doi:10.1002/jbmr.211 (2011).

36 Vainionpaa, A. *et al.* Intensity of exercise is associated with bone density change in premenopausal women. *Osteoporosis international : a journal established as result of cooperation between the European Foundation for Osteoporosis and the National Osteoporosis Foundation of the USA* **17**, 455-463, doi:10.1007/s00198-005-0005-x (2006).

37 Dickerson, D. A., Sander, E. A. & Nauman, E. A. Modeling the mechanical consequences of vibratory loading in the vertebral body: microscale effects. *Biomechanics and Modeling in Mechanobiology* **7**, 191-202, doi:10.1007/s10237-007-0085-y (2008).

38 Chan, M. E., Uzer, G. & Rubin, C. The Potential Benefits and Inherent Risks of Vibration as a Non-Drug Therapy for the Prevention and Treatment of Osteoporosis. *Current osteoporosis reports*, 1-9, doi:10.1007/s11914-012-0132-1 (2013).

39 Fritton, S. P., McLeod, K. J. & Rubin, C. T. Quantifying the strain history of bone: spatial uniformity and self-similarity of low-magnitude strains. *Journal of biomechanics* **33**, 317-325, doi:10.1016/s0021-9290(99)00210-9 (2000).

40 Marin-Cascales, E. *et al.* Whole-body vibration training and bone health in postmenopausal women: A systematic review and meta-analysis. *Medicine* **97**, e11918, doi:10.1097/md.0000000000011918 (2018).

41 Gilsanz, V. *et al.* Low-Level, High-Frequency Mechanical Signals Enhance Musculoskeletal Development of Young Women With Low BMD. *J.Bone Miner.Res.* **21**, 1464-1474 (2006).

42 Ritzmann, R., Stark, C. & Krause, A. Vibration therapy in patients with cerebral palsy: a systematic review. *Neuropsychiatric disease and treatment* **14**, 1607-1625, doi:10.2147/ndt.s152543 (2018).

43 Mogil, R. J. *et al.* Effect of Low-Magnitude, High-Frequency Mechanical Stimulation on BMD Among Young Childhood Cancer Survivors: A Randomized Clinical Trial. *JAMA Oncol*, doi:10.1001/jamaoncol.2015.6557 (2016).

44 Rubin, C. *et al.* Quantity and quality of trabecular bone in the femur are enhanced by a strongly anabolic, noninvasive mechanical intervention. *J Bone Miner Res* **17**, 349-357, doi:10.1359/jbmr.2002.17.2.349 (2002).

45 Rubin, C., Xu, G. & Judex, S. The anabolic activity of bone tissue, suppressed by disuse, is normalized by brief exposure to extremely low-magnitude mechanical stimuli. *FASEB J* **15**, 2225-2229, doi:10.1096/fj.01-0166com (2001).

46 Pongkitwitoon, S., Uzer, G., Rubin, J. & Judex, S. Cytoskeletal Configuration Modulates Mechanically Induced Changes in Mesenchymal Stem Cell Osteogenesis, Morphology, and Stiffness. *Scientific reports* **6**, 34791, doi:10.1038/srep34791 (2016).

47 Uzer, G. *et al.* Cell Mechanosensitivity to Extremely Low-Magnitude Signals Is Enabled by a LINCed Nucleus. *STEM CELLS* **33**, 2063-2076, doi:10.1002/stem.2004 (2015).

48 Uzer, G., Pongkitwitoon, S., Ete Chan, M. & Judex, S. Vibration induced osteogenic commitment of mesenchymal stem cells is enhanced by cytoskeletal remodeling but not fluid shear. *Journal of biomechanics* **46**, 2296-2302, doi:10.1016/j.jbiomech.2013.06.008 (2013).

49 Uzer, G. *et al.* Sun-mediated mechanical LINC between nucleus and cytoskeleton regulates betacatenin nuclear access. *Journal of biomechanics* **74**, 32-40, doi:10.1016/j.jbiomech.2018.04.013 (2018).

50 Thompson, M., Woods, K., Newberg, J., Oxford, J. T. & Uzer, G. Low-intensity vibration restores nuclear YAP levels and acute YAP nuclear shuttling in mesenchymal stem cells subjected to simulated microgravity. *NPJ microgravity* **6**, 35, doi:10.1038/s41526-020-00125-5 (2020).

51 Newberg, J. K., Schimpf, J., Woods, K., Davis, P. H. & Uzer, G. Isolated Nuclei Stiffen in Response to Low Intensity Vibration. *bioRxiv*, 2020.2004.2009.034546, doi:10.1101/2020.04.09.034546 (2020).

52 Coughlin, T. R. & Niebur, G. L. Fluid shear stress in trabecular bone marrow due to low-magnitude high-frequency vibration. *Journal of biomechanics* **45**, 2222-2229, doi:10.1016/j.jbiomech.2012.06.020 (2012).

53 Birmingham, E. *et al.* Mechanical stimulation of bone marrow in situ induces bone formation in trabecular explants. *Annals of biomedical engineering* **43**, 1036-1050, doi:10.1007/s10439-014-1135-0 (2015).

54 Uzer, G. *et al.* Separating Fluid Shear Stress from Acceleration during Vibrations In Vitro: Identification of Mechanical Signals Modulating the Cellular Response. *Cellular and Molecular Bioengineering* **5**, 266-276, doi:10.1007/s12195-012-0231-1 (2012).

55 Uzer, G. *et al.* Gap Junctional Communication in Osteocytes Is Amplified by Low Intensity Vibrations In Vitro. *PLoS ONE* **9**, e90840, doi:10.1371/journal.pone.0090840 (2014).

56 Silva, D. *et al.* Biocompatibility, biodegradation and excretion of polylactic acid (PLA) in medical implants and theranostic systems. *Chemical Engineering Journal* **340**, doi:10.1016/j.cej.2018.01.010 (2018).

57 Tack, P., Victor, J., Gemmel, P. & Annemans, L. 3D-printing techniques in a medical setting: a systematic literature review. **15**, doi:10.1186/s12938-016-0236-4 (2016).

58 Xu, X., Jha, A., Harrington, D., Farach-Carson, M. & Jia, X. Hyaluronic Acid-Based Hydrogels: From a Natural Polysaccharide to Complex Networks. *Soft matter* **8**, 3280-3294, doi:10.1039/C2SM06463D (2012).

59 Rubin, C. T. & Lanyon, L. E. Regulation of bone formation by applied dynamic loads. *The Journal of bone and joint surgery. American volume* **66**, 397-402 (1984).

60 Gurkan, U. A. & Akkus, O. The Mechanical Environment of Bone Marrow: A Review. **36**, doi:10.1007/s10439-008-9577-x (2008).

61 Jansen, L. E., Birch, N. P., Schiffman, J. D., Crosby, A. J. & Peyton, S. R. Mechanics of intact bone marrow. **50**, doi:10.1016/j.jmbbm.2015.06.023 (2015).

62 Rammohan, A. V., Lee, T. & Tan, V. B. C. A Novel Morphological Model of Trabecular Bone Based on the Gyroid. *International Journal of Applied Mechanics* **07**, 1550048, doi:10.1142/S1758825115500489 (2015).

63 Blaber, J., Adair, B. & Antoniou, A. Ncorr: Open-Source 2D Digital Image Correlation Matlab Software. *Experimental Mechanics* **55**, 1105-1122, doi:10.1007/s11340-015-0009-1 (2015).

64 Papageorgiou, M., Föger-Samwald, U., Wahl, K., Kerschan-Schindl, K. & Pietschmann, P. Age- and Strain-Related Differences in Bone Microstructure and Body Composition During Development in Inbred Male Mouse Strains. *Calcified tissue international* **106**, 431-443, doi:10.1007/s00223-019-00652-8 (2020).

65 Glatt, V., Canalis, E., Stadmeyer, L. & Bouxsein, M. L. Age-related changes in trabecular architecture differ in female and male C57BL/6J mice. *Journal of bone and mineral research : the official journal of the American Society for Bone and Mineral Research* **22**, 1197-1207, doi:10.1359/jbmr.070507 (2007).

66 Lassen, N. E. *et al.* Coupling of Bone Resorption and Formation in Real Time: New Knowledge Gained From Human Haversian BMUs. *J Bone Miner Res* **32**, 1395-1405, doi:10.1002/jbmr.3091 (2017).

67 Delaisse, J. M. *et al.* Re-thinking the bone remodeling cycle mechanism and the origin of bone loss. *Bone* **141**, 115628, doi:10.1016/j.bone.2020.115628 (2020).

68 Dupont, S. *et al.* Role of YAP/TAZ in mechanotransduction. *Nature* **474**, 179-183, doi:http://www.nature.com/nature/journal/v474/n7350/abs/10.1038-nature10137-unlocked.html#supplementary-information (2011).

Figure 1

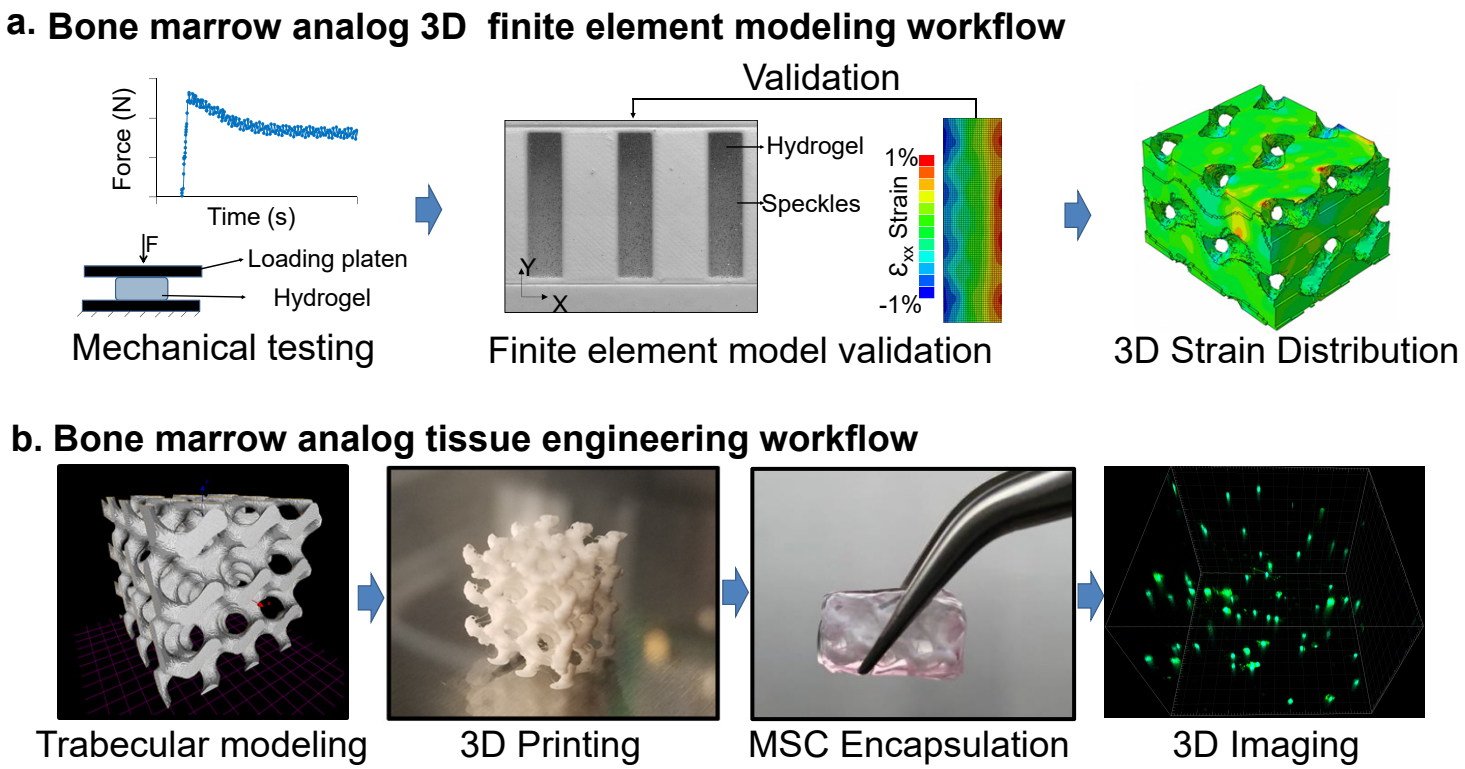

Figure 1. Experimental Design

Figure 2

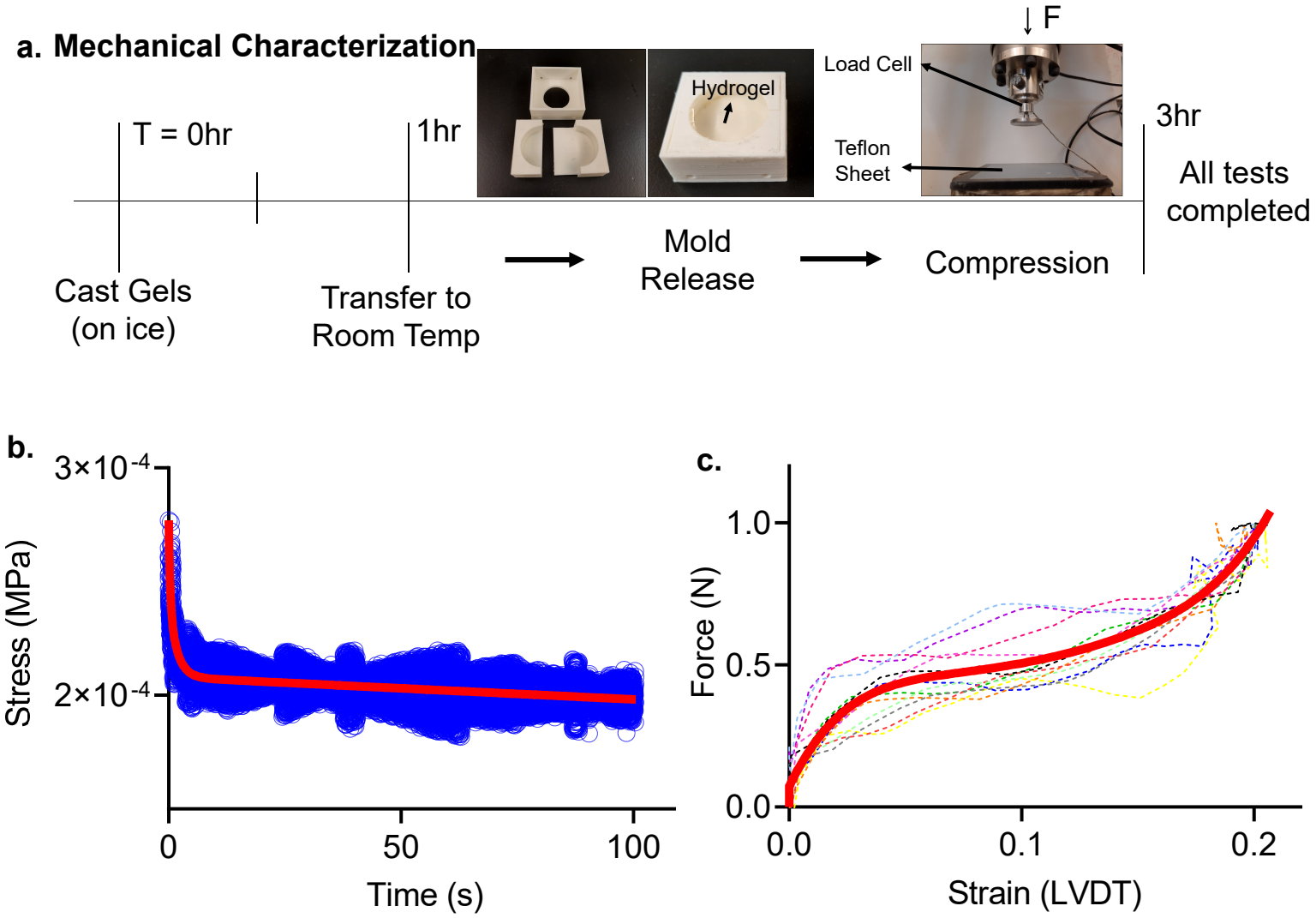

Figure 2. Mechanical Characterization Setup. a) Timeline of the compression testing, with all tests completed within 3 hours of initial gelation for the calibration gels. 3D printed mold used to cast instantaneous gel pucks (24mm internal diameter, and a height of 9mm). Experiments were completed using an INSTRON ElectroPuls E10000 using a 10N load-cell. The sample rested on a Teflon coated sheet lightly coated in water to prevent adherence. **b)** Relaxation data over a 100 second time period (blue) and the resulting fit line (red) relaxing from 2.8×10^{-5} MPa and reaching long term relaxation at approximately 2.1×10^{-5} Mpa. **c)** Instantaneous ramp data from 12 trials (dotted 5th order polynomial fit (blue), compressed to 0.2 strain (10.8 mm/s).

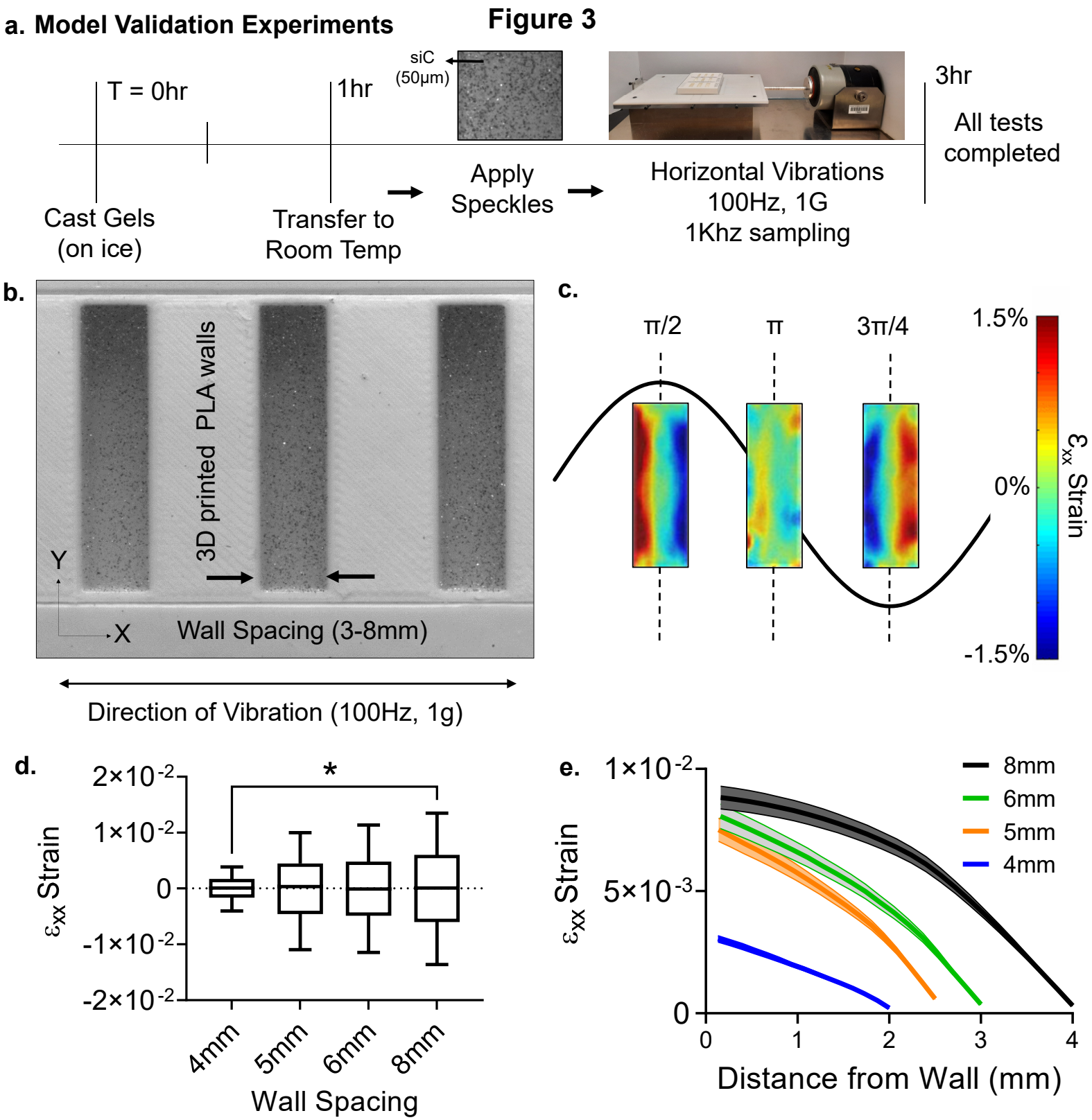

Figure 3. Model validation experiments. a) Timeline of the DIC tests, with all tests completed within 3 hours of initial gelation for the calibration gels. Hydrogels were speckled with 220 grid SiC and the camera recorded the motions at 2000 frames per second (fps). Horizontal vibration plate was driven by Labworks ET-126HF-1,-4 (13lbf) Electrodynamic transducer **b)** A PLA experimental setup was manufactured to visualize strain during100Hz -1g vibrations at the horizontal direction. ε_{xx} strains varied periodically with the maximum value of 0.015 at 8mm spacing **c)** As the spacing decreased 62% to 4mm ε_{xx} strain decreased by two orders of magnitude showing a positive, non-linear correlation in the average maximum of the strain **d)** Mapping max strain magnitudes from the wall to the mid-point showed a convex parabolic strain profile that minimized at the middle.

Figure 4

a.

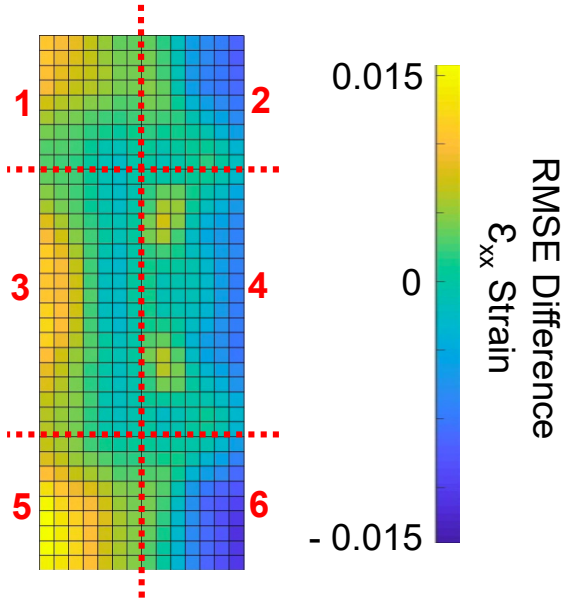

b.

Region of Interest	Absolute Average RMSE Difference
1	7.7×10^{-3}
2	7.9×10^{-3}
3	4.7×10^{-3}
4	5.2×10^{-3}
5	11.3×10^{-3}
6	12.2×10^{-3}

Figure S4 RMSE difference between DIC and FE strains . a) The difference between the surface of DIC experimental and the FE model was measured with a 15x37 grid and divided into 6 regions for comparison. Most of the difference occurs on the outside, especially the outer edges. **b)** Largest difference of 0.015 of averaged ε_{xx} magnitude difference occurs in the regions 5 and 6. Regions 3 and 4 are the closest matching, with an averaged ε_{xx} magnitude difference of 0.0047 and 0.0052, respectively. The corner regions (1, 2, 5 and 6) has an averaged ε_{xx} magnitude difference of 0.0077, 0.0079, 0.0113, and 0.0122, respectively.

Figure 5

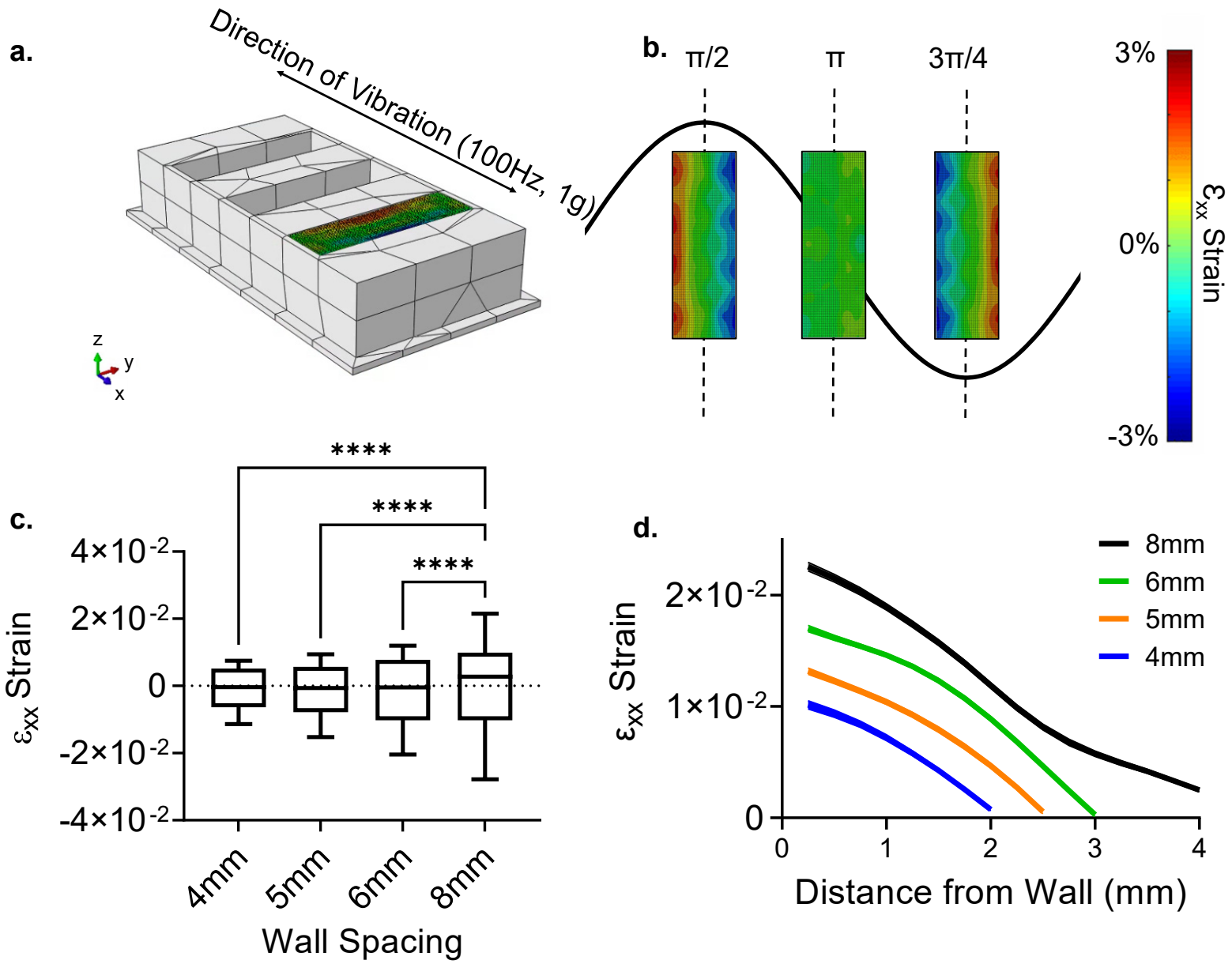

Figure 5. Model validation simulations a) Finite Element (FE) model setup with 8mm wall spacing. Wells were vibrated identically to the experiments (Fig.3). Each FE run was proceeded by a gravity step **b)** ε_{xx} strain magnitude over the cycle. maximum ε_{xx} values were symmetrical at both the π/2 and 3π/4, in addition to both ends of the well, demonstrating steady state **c)** . Extrema differences were evenly spaced as the spacing changes. When compared, the surface strain at the 8mm between the averaged maximum ε_{xx} strains of 6mm, 5mm and 4mm well widths decreased to 0.017±0.00040 (-22%, $p<0.05$), 0.013±0.00030 (41%, $p<0.05$), 0.010±0.00037 (-54%, $p<0.05$) , and 0.0026±0.00051 (-88%, $p<0.05$), **d)** Mapping the maximum strain magnitudes, we see a convex parabolic curve with each spacing, excluding 8mm.

Figure 6

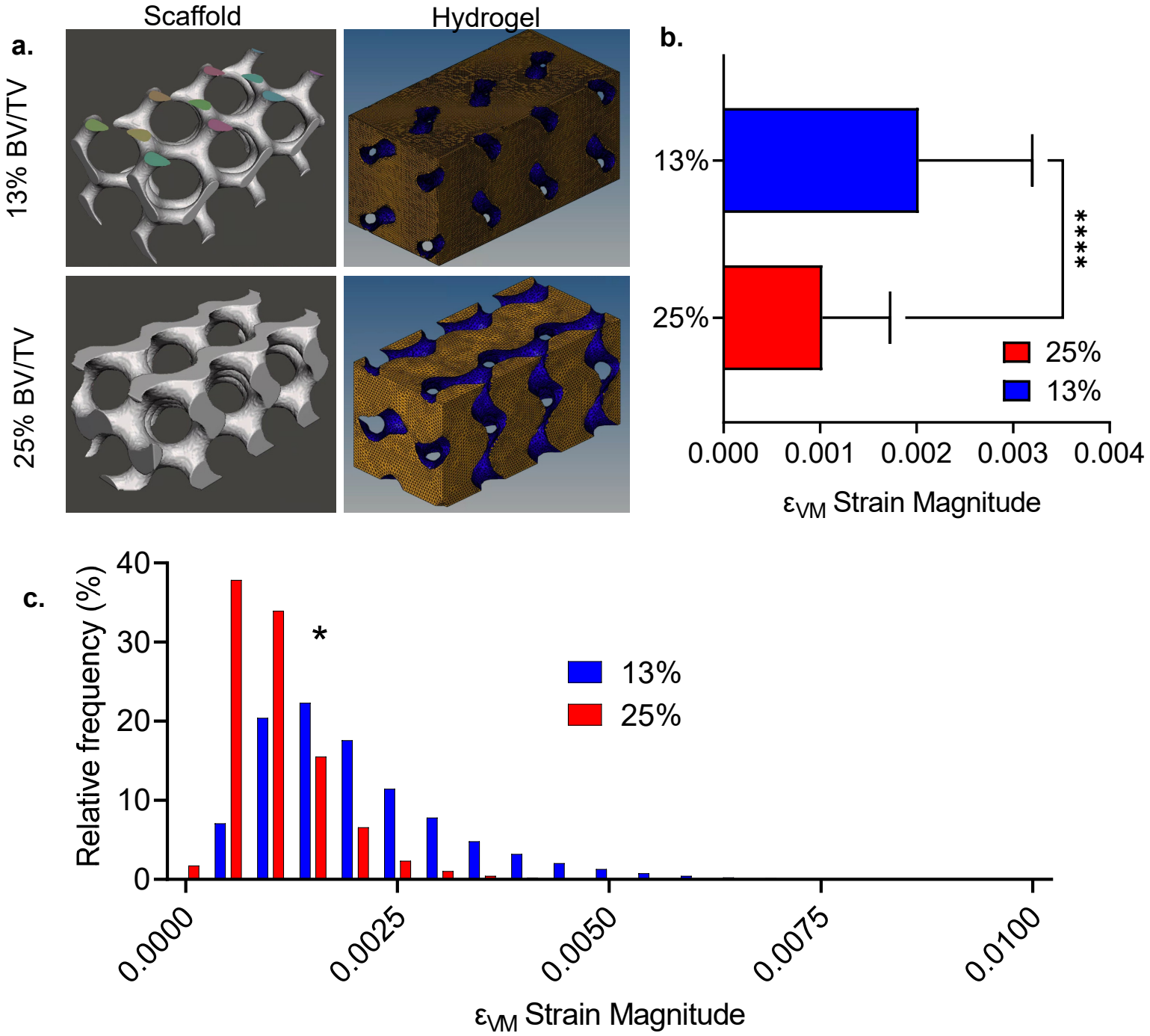

Figure 6. Low trabecular volumes increase LIV-induced hydrogel strains. a) We compared the 3D strain distribution between 13% and 25% scaffolds under LIV using HA gel mechanical properties (Table S1). **b)** Comparing the Von Mises strain (ε_{VM}) magnitude averaged over steady state cycles showed that εVM of 13% was almost doubled when compared to 25% scaffold ($p<0.0001$). **c)** ε_{VM} distribution indicated normally distributed strains for both 13% and 25% scaffolds. Histograms of 25% and 13% scaffolds were statistically different ($p<0.05$)., 25% scaffold had more elements with lower strain values while 13% scaffold showed elements with higher ε_{VM} strains. Comparison of individual strain components were presented in Fig.S4 & S5.

Figure 7.

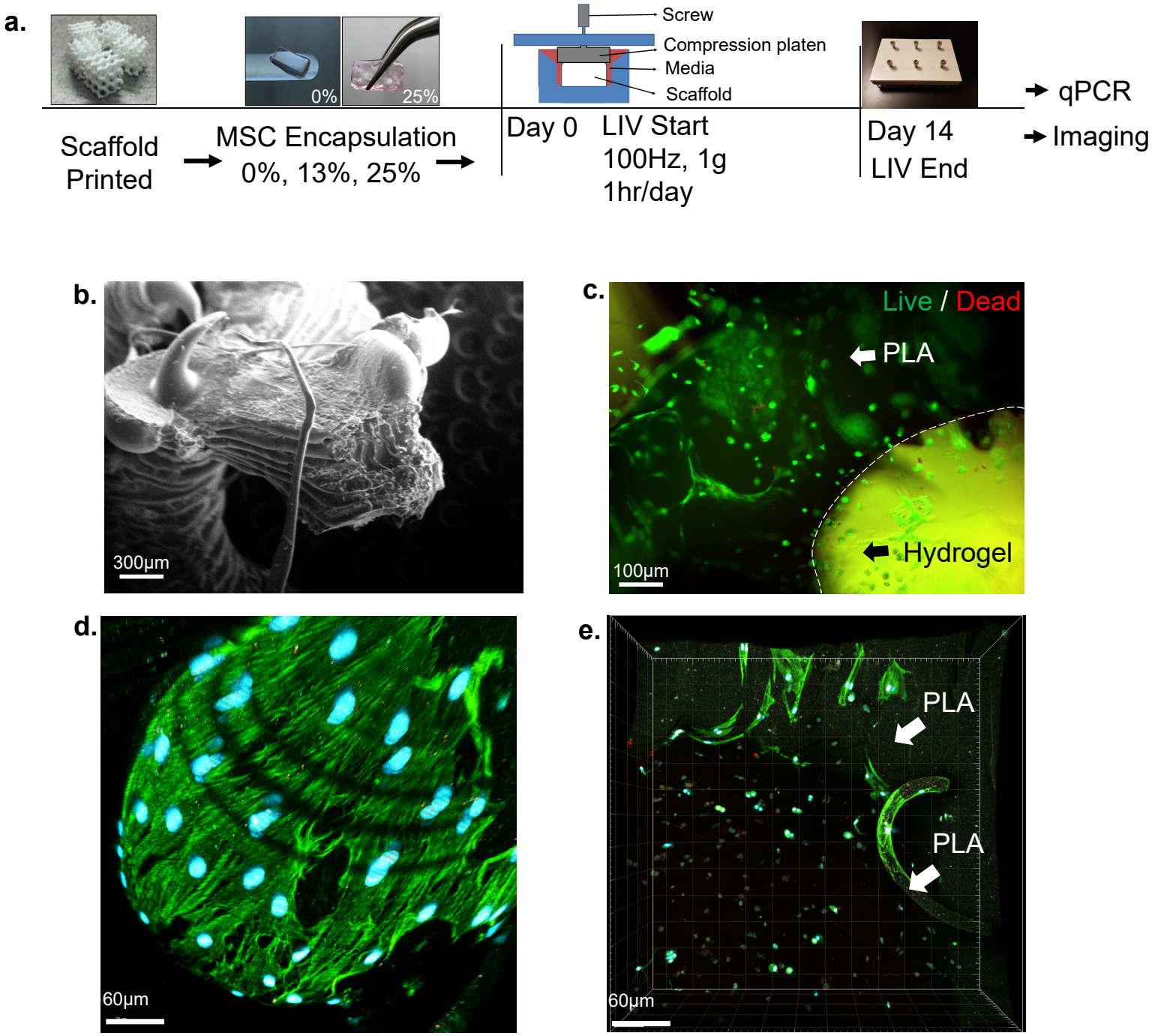

Figure 7. Bone Analogs show viable cells with two distinct cell populations. a) Two sets of PLA scaffolds (13% and 25% volume fill) and 0% controls were generated. Cell-laden 13% and 25% scaffolds were vibrated one hour every day at room temperature using 100 Hz frequency and 1g acceleration magnitude outside of the incubator. After 14 days, samples were allocated for qPCR (N=4 scaffolds/grp), imaging (N=3 scaffolds/grp). **b)** PLA surface provides an ideal surface for cell attachment **c)** Utilizing live/dead straining to detect cell viability prior to start of the experiments at 7 days post-encapsulation showed viable cells on both PLA and in hydrogels. **d)** Morphology of cells on PLA surfaces were similar to 2D culture plates (Fig.S5), showing elongated morphology while cells in **e)** hydrogels were smaller and more rounded.

Figure 8

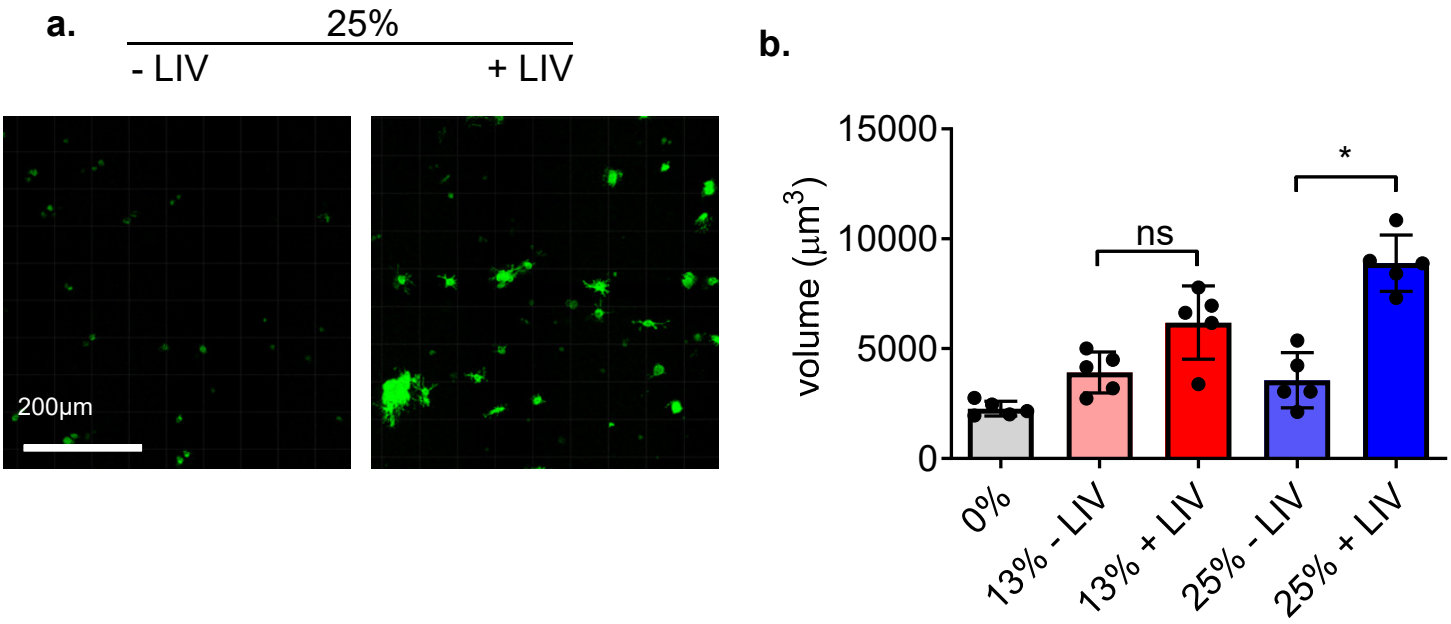

Figure 8. LIV increases F-actin volume F-actin staining in **a)** 25% scaffolds b show increased F-actin volume in +LIV samples when compared to controls (-LIV). **b)** Quantification F-actin volume showed no change in -LIV groups. 13% +LIV groups had a trend toward increased F-actin and 25% +LIV group showed 2.5-fold increase in F-actin volume ($p<0.05$).

Figure 9

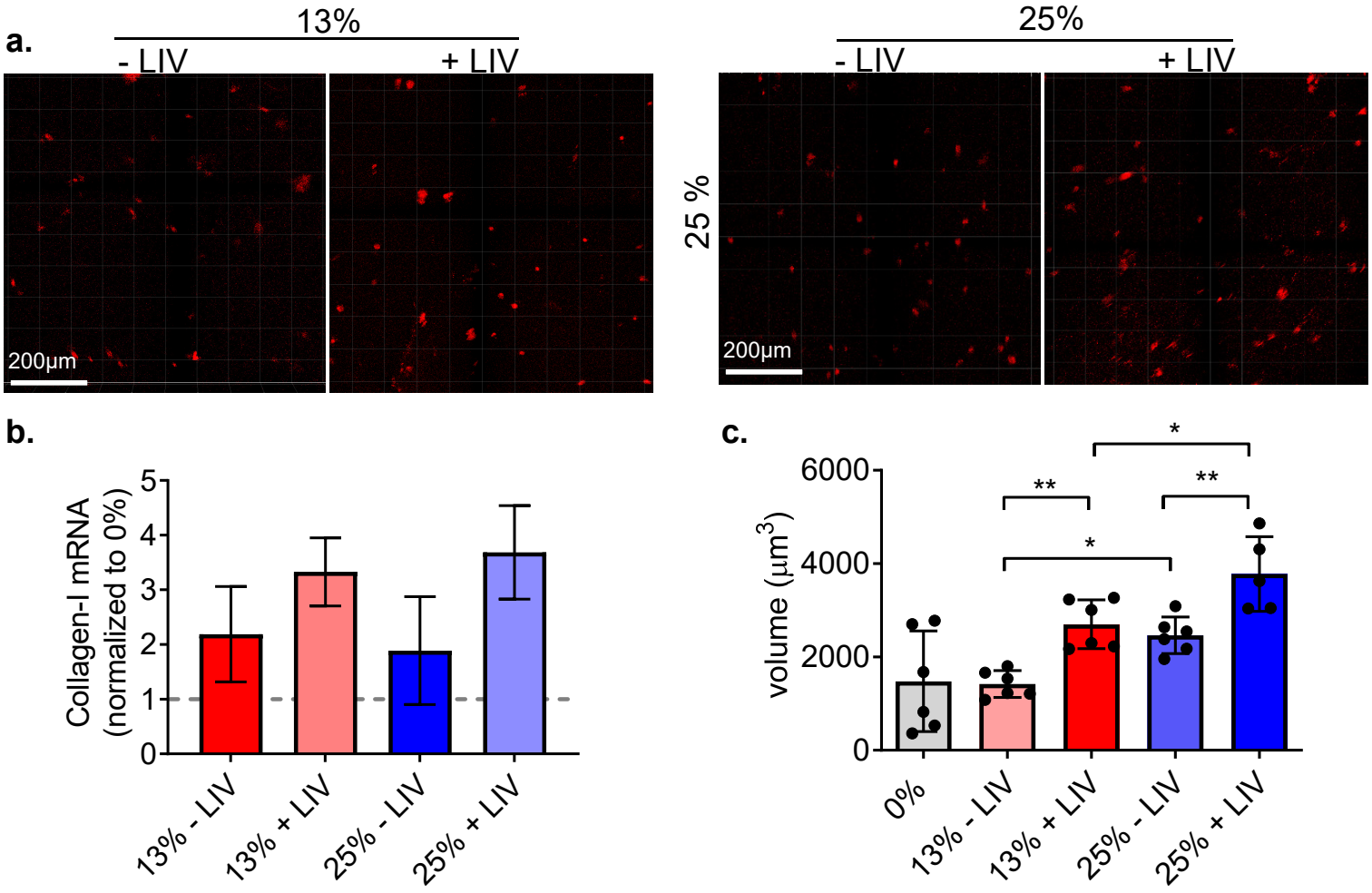

Figure 9. Trabecular volume differentially regulates basal and LIV-induced regulates collagen-I production Collagen-I immunostaining in **a)**13% and 25% scaffolds show an increased collagen labeling in vibrated samples (+LIV), vs non vibrated controls (-LIV). **b)** Collagen-I mRNA quantification show an increasing trend of collagen-I expression in +LIV samples (+50% in 13% and +94% in 25% samples. Everything was normalized to 0% controls (shown as the dashed gray bar) **c)** Quantification Collagen-I volume showed unchanged basal collagen-I levels between 0% and 13% controls while -LIV 25% group had a 73% increase compared to -LIV 13% group ($p<0.05$). LIV increased Collagen-I in both 13% and 25% groups by 87% and 53% respectively ($p<0.01$) and +LIV 25% remained significantly higher compared to +LIV 13% group (37%, $p<0.05$).

Increased deformations of aging bone marrow during physical activity is dispensable for cell mechanoresponse in bone analogs

Alex Regner[1*], Maximilien DeLeon[2*], Sean Howard[1], Kalin Gibbons[1], Derek Nesbitt[1], Trevor Lujan[1], Clare Fitzpatrick[1], Mary C Farach-Carson [2], Danielle Wu[2], Gunes Uzer[1 †]

[1] Mechanical and Biomedical Engineering Department, Boise State University

[2] Department of Diagnostic and Biomedical Sciences, UTHealth Science Center at Houston

*co-first author, †Corresponding author

Supplementary Figures

Figure S1

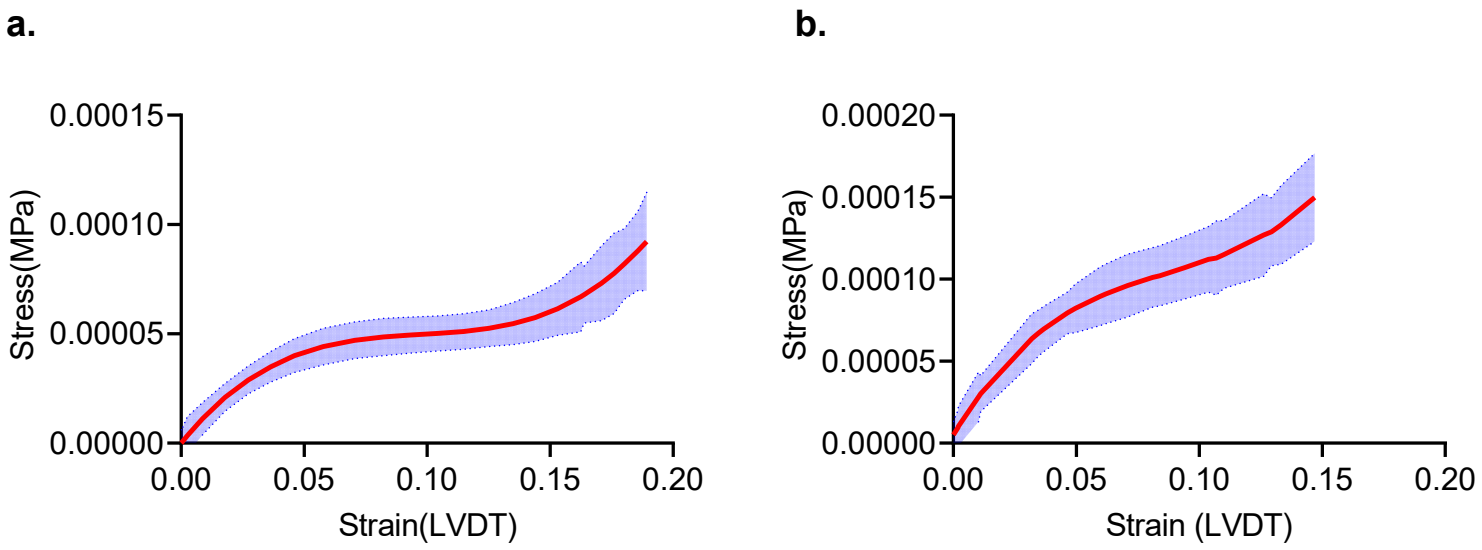

Figure S1. Stress-strain curves for the **a)** calibration and **b)** HA gels from instantaneous compression tests.

Figure S2

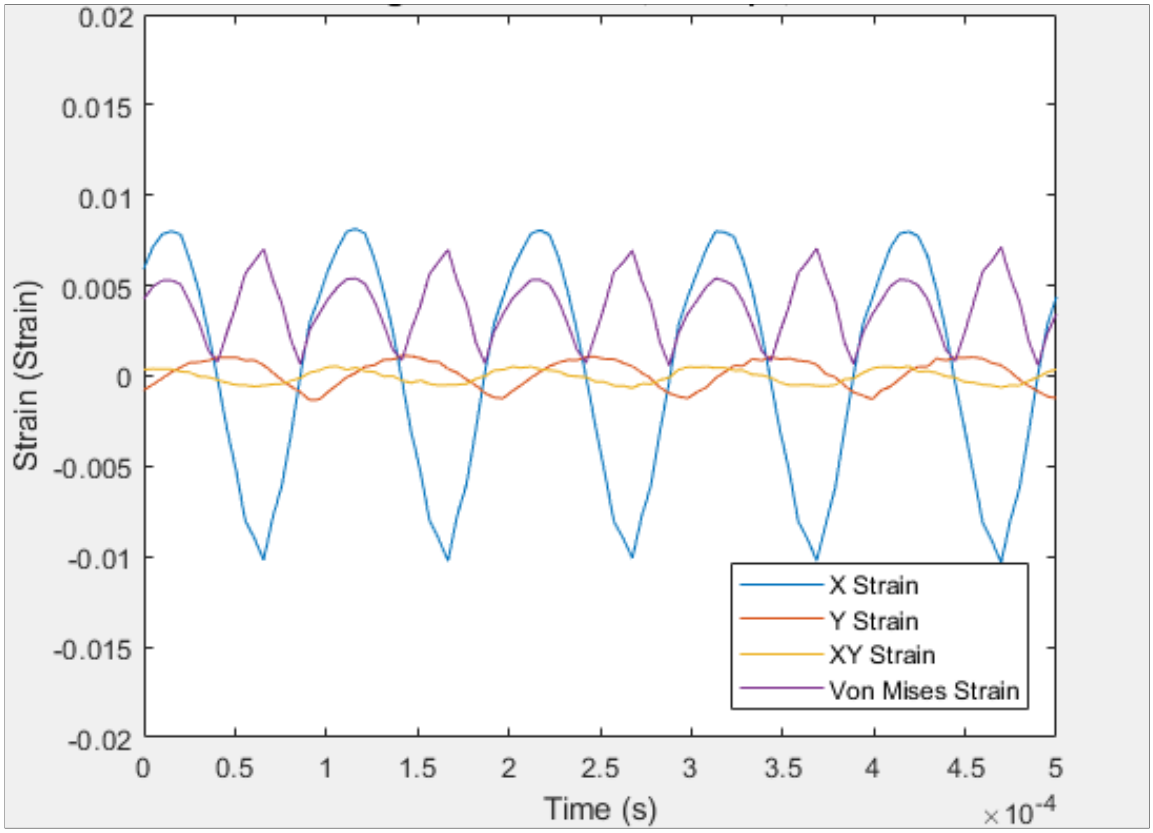

Figure S2. Calibration gel strains were compared during horizontally applied LIV stimulation along x-direction. The ε_{xx} strain was found to be at least one order of magnitude larger than ε_{yy} or ε_{xy}.

Figure S4

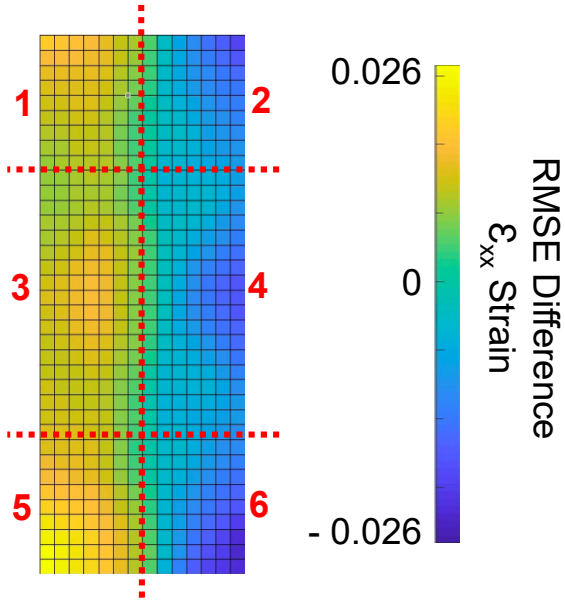

Region of Interest	Absolute Average RMSE Difference
1	11×10^{-3}
2	10×10^{-3}
3	9.1×10^{-3}
4	10×10^{-3}
5	9.8×10^{-3}
6	24×10^{-3}

Figure S4. a) The difference between the surface of DIC experimental and the FE model was measured with a 15x37 grid and divided into 6 regions for comparison. Most of the difference occurs on the outside, especially the outer edges. **b)** The largest difference of 0.024 again occurs in region 6, with regions 3 and 4 matching the closest with ε_{xx} averages of .0091 and 0.0082, respectively. The corner regions had average differences of 0.011, 0.010, 0.010, and 0.098 for 1, 2, 4, & 5 respectively.

Figure S5

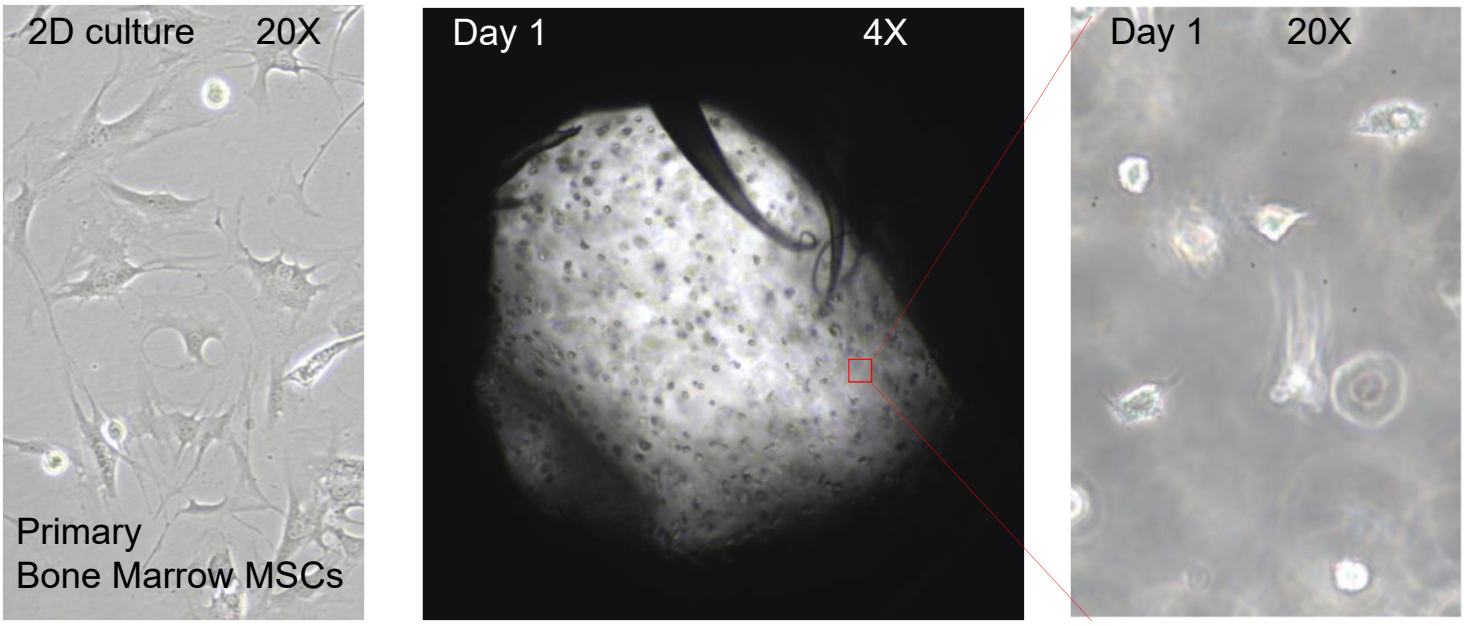

Figure S5. Prior to encapsulation MSCs show elongated morphology on 2D culture plastic. 24hr after the cell encapsulation, MSCs are largely retained within the hydrogel (4X) and show some elongation, suggesting active migration (20x).